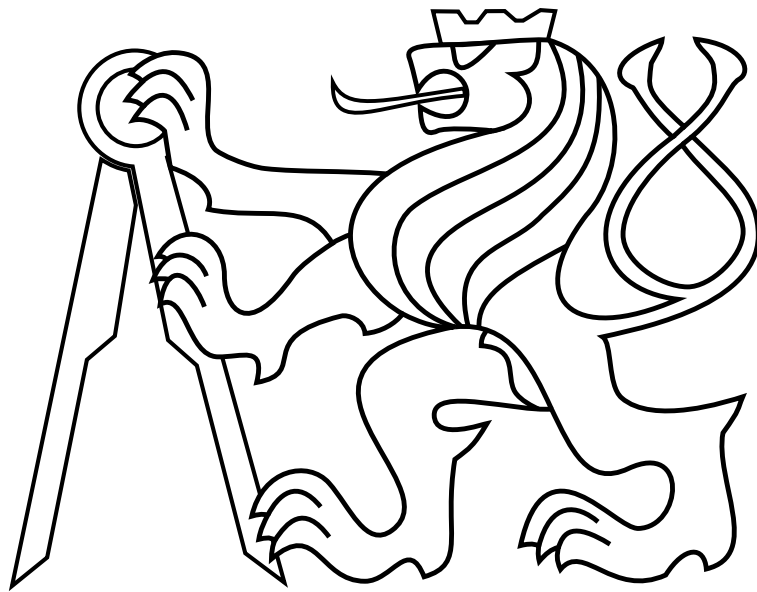CZECH TECHNICAL UNIVERSITY IN PRAGUE

Faculty of Electrical Engineering

BACHELOR'S THESIS

**Design of a Specialized UAV Platform for the Discharge of a
Fire Extinguishing Capsule**

Vojtěch Nydrle

Thesis supervisor: **Ing. Pavel Petráček**

Department of Cybernetics

AUGUST 2020

I declare that the presented work was developed independently and that I have listed all sources of information used within it in accordance with the methodical instructions for observing the ethical principles in the preparation of university theses.

In Prague on ....

BACHELOR'S THESIS ASSIGNMENT

I. Personal and study details

Student's name: **Nydrle Vojtěch** Personal ID number: **474408**

Faculty / Institute: **Faculty of Electrical Engineering**

Department / Institute: **Department of Cybernetics**

Study program: **Cybernetics and Robotics**

II. Bachelor's thesis details

Bachelor's thesis title in English:

Design of a Specialized UAV Platform for the Discharge of a Fire Extinguishing Capsule

Bachelor's thesis title in Czech:

Návrh specializované bezpilotní helikoptéry pro vystřelování ampulí k hašení požárů

Guidelines:

The aim of this thesis is to design and construct a specialized unmanned aerial vehicle (UAV) suited for aerial discharge of fire extinguishing capsules (e.g., [1]) and to detect fires with an onboard thermal camera. The following tasks will be solved:
1) Design and construct a UAV that respects requirements of the dynamic influence originating from horizontal discharging of an onboard payload with 0.5-1kg weight.
2) Integrate a launcher for discharging fire extuingishing capsules [1, 2] onto the designed aerial platform. The launcher will be either provided by an external supplier or its proof-of-concept placeholder will be designed by the student.
3) Familiarize yourself with the system of Multi-Robot Systems group for stabilization and control of UAVs [3].
4) Design an algorithm to detect fires from an onboard thermal camera [4, 5].
5) Design an algorithm to autonomously position the UAV in order to launch the fire extuingishing capsules into a detected fire [2, 4].
6) Perform a real-world experiment and analyze the functionality of the capsule-launching mechanism and of the developed fire detection algorithm in real-world conditions.

Bibliography / sources:

[1] Fire Defender Systems, Bonpet Ampoule, Online: http://www.fire-defender.com/en/bonpet-3/1465-2/ (Visited on 10/1/2020).
[2] D. Heřt. "Autonomous Predictive Interception of a Flying Target by an Unmanned Aerial Vehicle", Master's Thesis, FEE CTU, 2018.
[3] V. Spurný, T. Báča, M. Saska, R. Pěnička, T. Krajník, J. Thomas, D. Thakur, G. Loianno and V. Kumar. Cooperative Autonomous Search, Grasping and Delivering in a Treasure Hunt Scenario by a Team of UAVs. Journal of Field Robotics, 2018.
[4] Merino, Luis et al. "Automatic Forest Fire Monitoring and Measurement using Unmanned Aerial Vehicles." (2010).
[5] Che-Bin Liu and N. Ahuja, "Vision based fire detection," Proceedings of the 17th International Conference on Pattern Recognition, ICPR 2004, Cambridge.

Name and workplace of bachelor's thesis supervisor:

Ing. Pavel Petráček, Multi-robot Systems, FEE

Name and workplace of second bachelor's thesis supervisor or consultant:

Date of bachelor's thesis assignment: **10.01.2020** Deadline for bachelor thesis submission: **14.08.2020**

Assignment valid until: **30.09.2021**

_____ _____ _____
Ing. Pavel Petráček doc. Ing. Tomáš Svoboda, Ph.D. prof. Mgr. Petr Páta, Ph.D.
Supervisor's signature Head of department's signature Dean's signature

III. Assignment receipt

The student acknowledges that the bachelor's thesis is an individual work. The student must produce his thesis without the assistance of others, with the exception of provided consultations. Within the bachelor's thesis, the author must state the names of consultants and include a list of references.

_____._____   _____
Date of assignment receipt   Student's signature

Acknowledgments

I would like to thank my thesis adviser, for his advice and improvements which was very helpful for this work also for his patience and goodwill. I would also like to thank all MRS group for their help with experiments and useful advice, also for the opportunity to do the project. Last thanks belong to my family for their support.

Sincerely, thank you

Abstract

This thesis deals with the design of an unmanned multirotor aircraft system specialized for autonomous detection and localization of fires from onboard sensors, and the task of fast and effective fire extinguishment. The main part of this thesis focuses on the detection of fires in thermal images and their localization in the world using an onboard depth camera. The localized fires are used to optimally position the unmanned aircraft in order to effectively discharge an ampoule filled with a fire extinguishant from an onboard launcher. The developed methods are analyzed in detail and their performance is evaluated in simulation scenarios as well as in real-world experiments. The included quantitative and qualitative analysis verifies the feasibility and robustness of the system.

Keywords: unmanned aerial vehicle, fire detection, fire localization, semi-autonomous fire extinguishing, horizontal aerial discharge, tall-building fire extinguishing

Abstrakt

Tato práce se zabývá návrhem systému specializovaného pro autonomní detekci a lokalizaci požárů z palubních senzorů bezpilotních helikoptér. Hašení požárů je zajištěno automatickým vystřelením ampule s hasící kapalinou do zdroje požáru z palubního vystřelovače. Hlavní část této práce se soustředí na detekci požárů v datech termální kamery a jejich následnou lokalizaci ve světě za pomoci palubní hloubkové kamery. Bezpilotní helikoptéra je poté optimálně navigována na pozici pro zajištění průletu ampule s hasící kapalinou do zdroje požáru. Vyvinuté metody jsou detailně analyzovány a jejich chování je testováno jak v simulaci, tak současně i při reálných experimentech. Kvalitativní a kvantitativní analýza ukazuje na použitelnost a robustnost celého systému.

Klíčová slova: bezpilotní helikoptéra, detekce ohně, lokalizace ohně, semi-automnomní hašení požárů, výstřel v letu, hašení požárů výškových budov

Contents

List of Figures

List of Tables

Chapter 1: Introduction

Contents

Extinguishment of fire in aboveground floors brings many difficulties, with the most significant being limited access for firemen to aboveground floors of the building. They often need to use ladders and enter the floor through a window, taking a lot of time while the fire may continue to grow. Usage of an unmanned aerial vehicle (UAV) for quick access to the window to begin extinguishment can reduce the growth of the fire and provide the time necessary for firemen to access the floor.

This thesis aims to design a UAV suitable for extinguishing fires in above-ground floors of buildings. The key use of this UAV is to extinguish fires through windows and the surrounding area to provide access to the floor and decrease the fire growing ratio. The UAV can be also used for investigating the floor or searching for survivors, but the fundamental purpose is to extinguish fires in the interior of the building from the exterior.

The Unmanned Aerial Vehicle is a kind of aircraft without a pilot on board, such as a remote-controlled airplane or multicopter, but can be controlled autonomously by an onboard computer. Multicopters can quickly land and take off vertically from various places making them useful in countless applications, such as monitoring, photography, cargo transport, investigating dangerous areas, and even elimination of unauthorized aircraft. The typical multicopter (see Figure 1.1) consists at least of three motors with propellers forcing air under the aircraft, platform for battery, electronics necessary for stabilization and navigation, and landing equipment. The variety of multicopters is extensive in size, count of rotors, and the rotors configuration.

The multicopter is ideal for firefighting purposes because of its ability to vertically land and take off almost anywhere. Usage of UAV in firefighting procedures reduces the risk to human lives while investigating burning objects or accessing fire sources. The UAV can also do many automatic operations faster than its human operator, for example, it can quickly return to the base for exhauster refilling or it can autonomously present the fire for exhausting. Small-sized UAV also has an advantage in accessing places dangerous or hardly accessible for humans.

Bonpet capsules [3] provide an effective automatic fire exhausting system. These capsules are mounted on walls and ceilings, when the temperature of the Bonpet liquid in the capsule rises to 90 °C the capsule breaks and deploys the liquid in its neighborhood. In the liquid begins an endothermic chemical reaction that cools down the area while chemicals in this liquid are decomposed into gases (CO_2, N_2). The remaining liquid protects the surface from re-ignition. When all of the liquid is decomposed to gas, no cleaning is needed. This liquid does not cause damage to electronics, human health, or the environment. One 600 ml Bonpet capsule can autonomously protect 8 m³ area.

The Bonpet liquid is also filled in an ampoule [4] designed for manual fire extinguishing by throwing it to the fire. This ampoule breaks from the temperature increase or when it falls. Therefore, this kind of ampoule is ideal for aerial discharge into the fire through a window from the UAV. The design of the UAV specialized for the aerial discharge of the ampoule to the fire is the main purpose of this thesis.

1.1 Motivation

Fire extinguishing in high-rise buildings is a difficult and dangerous operation where each second determines success. Fire exhausting in above-ground floors is complicated by narrow access to the fire sources and water distribution problems [5]. Solving these problems is time-consuming while the fire can completely burn down a room in several minutes [6]. Starting extinguishing too slowly leads to quick propagation of the fire and huge damage to the building construction. In extreme cases, the damages on the building can lead to its collapse.

Finding access to the fire source on high floors and investigating the burning building is extremely dangerous for the firemen and can impact their health or cause many kinds of injury. Falling objects can injure a fireman or obstruct his position to some room, where proximity to the fire may result in inhalation of smoke causing health problems [7]. Loss of the UAV in these conditions is a much acceptable result. For access to low floors, ladder tracks are commonly used, but the reachable height of the ladders is insufficient for many buildings.

The main motivation for this thesis is therefore to help save human lives, health, and possessions by applying the UAV for fire extinguishing in the above-ground floor of buildings

Figure 1.1: Photo of the designed, constructed, and tested UAV for the application in (semi)-autonomous fire-extuinguishing scenarios.

or places inaccessible to firemen. This UAV brings the possibility to quickly begin semi-automatic fire extinguishing to prevent fire propagation before the fireman can access the fire. The UAV can also provide information to the firemen about the fire's scope and presence of people in the affected area. In the case of a burning building with a fire present on stairs, this information can be very helpful for planning a fire-fighting strategy.

1.2 Related work

In recent years, UAVs are being used for many thermal monitoring applications such as power plant inspections [8, 9] and human and fire detection [10] leading to the tracking of wildfires [11–13] to help with its reduction. Solving the problem of tracking wildfires brings many approaches for fire detection and localization from various sensors. Many approaches use thermal cameras [14–19] while others use cameras monitoring in the visible spectrum with more complex algorithms for detection [20–24]. But even methods combining thermal and visual images were developed [25]. Some of these approaches to fire detection can be adapted for this semi-automatic fire extinguishing system.

Some special equipment for accessing the high floors of buildings has been developed [26–28]; these machines climb on building balconies or preventatively installed rails. A specialized helicopter was developed for eliminating fire through windows to enable access with ladders or by previously mentioned machines [29].

Another paper discusses scenarios using UAV for fire fighting [30, 31] describing mostly the strategy of the UAV-fire flight and its trajectory planning and optimization. In these scenarios, a team of UAVs cooperates with firemen to suppress the fire.

For the UAV, carrying an effective fire extinguisher is the most challenging due to the weight of the fire extinguisher and the limited power of the UAV. A special solution to this problem was created by supplying permanent extinguishant and power through a system tethering the UAV to the ground [32]. Another fire fighting UAV for exhausting wildfires drops balls filled with fire extinguishant into the fire [33]. Additionally, a UAV that can handle indoor fires have been developed. These UAVs are also designed for investigation of the burning building interior and searching for survivors [34, 35].

Our design also implements relative localization of the fire and horizontal discharge of the cargo to the localized object. This challenge of optimal UAV positioning is similar to game theory applications where a UAV protects a specific area against other intruder UAV [36]. The problem of cargo discharge was solved for wildfire exhausting [37], but also autonomous interception of a flying target [38]. The localization problem is often solved as localization of objects with known dimensions [39] or with the usage of neural networks [40, 41], or using stereo vision [36, 42, 43].

1.3 Outline

At the beginning of this thesis in Chapter 2, the characteristics of the operating environment of the UAV and its influence on the UAV construction are discussed. This chapter also discusses the challenges and difficulties that can occur and must be solved. In Chapter 3,

the design of the specialized UAV platform to cope with all these challenges is discussed. Chapter 4 looks at the design of algorithms for fire detection and positioning of the UAV to discharge the ampoule into the detected fire. This chapter also provides insights into the methodology of thermal imaging. At the end of this thesis in Chapter 5, results, and methodology of experiments to determine the quality of the designed systems are discussed.

1.4   Mathematical notation

Summary of mathematical notation used throughout the thesis is presented in Table 1.1.

Symbol	Example	Description
upper or lowercase letter	m, M, M	a scalar
bold upper or lowercase letter	$\mathbf{R}$, $\mathbf{h}$	a matrix
calligraphic upper letter	$\mathcal{T}$	a set or structure
lowercase letter accented by an arrow	$\vec{x}$	a column vector
upper index T	$\mathbf{R}^T$, $\vec{x}^T$	vector and matrix transpose
lower index	M_k, $\mathbf{R}_k$, $\mathcal{T}_k$, $\vec{x}_k$	M, $\mathbf{R}$, $\mathcal{T}$, $\vec{x}$ at discrete step k

Table 1.1: Overview of the mathematical notation.

1.5   Table of symbols

Chapter	Symbol	Description
Non-contact temperature measurement (Section 4.1.1)	M_e	Radiant exitance
	T	Temperature
	ε	Emissivity
	σ	Stefan–Boltzmann constant
	ν	Radiation frequency
	k_B	Boltzmann constant
	h	Planck constant
	c	Speed of light
	b	Wien's displacement constant
	E_e	Irradiance
	Φ_e	Radiant flux
Fire detection in thermal images (Section 4.1.2)	T_t	Temperature threshold
	$\mathcal{I}$	Thermal image
	i	Fire hypothesis index
	$\mathcal{T}_i$	Fire hypothesis
	d_i	Distance of objects seen be pixel i
	α	Camera's FoV
	S	Image dimension

Chapter	Symbol	Description
	A_i	Fire hypothesis area
	N_i	Fire hypothesis pixel area
Projection of fire detections to world (Section 4.2.2)	$\mathbf{C}$, $\mathbf{C}_d$, $\mathbf{C}_t$	Camera projection matrix
	$\mathbf{T}$, $\mathbf{T}_t^d$, $\mathbf{T}_d^l$	Transformation matrix
	$\mathcal{O}$, $\mathcal{O}_t$, $\mathcal{O}_d$, $\mathcal{O}_l$	Coordinations frames
	$\mathcal{O}^I$, $\mathcal{O}_t^I$, $\mathcal{O}_d^I$	Image plane coordinations frames
	$\vec{x}_t$, $\vec{x}_d$, $\vec{x}_l$	Coordinates of point X in different frames
	$\vec{x}_t^I$, $\vec{x}_d^I$	Projection of point X to different cameras
	X	Fire hypothesis position
	$\mathcal{Q}$	Surface seen by camera
	$\mathcal{R}$, $\mathcal{X}$, $\mathcal{Y}$	Set of possible solutions
	$\vec{u}$	Vector pointing to X
	$d(\vec{v})$	depth measured on pixel $\vec{v}$
Fire localization algorithm (Section 4.2.3)	r_m	Maximum measurement range
	r_d	Discretization resolution
	j, k, l	Sample index
	m_j	Depth sample
	$\mathcal{S}$, $\mathcal{M}$, $\mathcal{V}$, $\mathcal{W}$	Set of possible solutions
Fire locking (Section 4.3)	t	Time
	$\vec{p}(t)$	Position in time t
	h	Coefficient of friction
	m	Mass
	g	Gravitational acceleration of Earth
	v_0	Muzzle velocity
	l_h, l_v	Horizontal and vertical position

Table 1.2: Summary of symbols utilized throughout Chapter 4.

Chapter 2: Preliminaries

Contents

The aim of this thesis is a design of a complete autonomous UAV system for aerial discharge of fire extinguishing capsules into real-world fires. The system consists from design of:

- a specialized UAV platform capable of sustaining significant dynamic recoil and

- a fire detection system capable of fire analysis, fire localization, UAV navigation, and effective discharge of fire extinguishing capsules.

This aerial system brings in the ability to exhaust fires fast, semi-autonomously, and in places hardly accessible by a human, such as above-ground floors of buildings. That means that the UAV can be deployed nearby burning fires by a pilot operating the system from a safe distance from the certain danger. The application goal is to assist the operator with detection and localization of the fires with onboard sensors, position the UAV appropriately, and blast a fire extinguishing capsule into the fire. The UAV mission consists of two parts - an operator-controlled navigation of the UAV to close proximity of the fire and autonomous fire localization and discharge of extinguishing capsule to the fire.

The specific operation environment brings up several challenges, which need to be accounted for during the system design. These difficulties can affect the functionality of some sensors, actuators, electronics, and mechanical parts. Overcoming these challenges is necessary in order to design a robust and reliable system, which can be used in real-world applications.

2.1 Fire detection system

One possible scenario of UAV usage is operator-controlled flight around the burning building with continuous fire detection followed by automatic UAV positioning for the discharge of the fire exhausting capsule from the exterior of the building to the fire detected either in interior or exterior of the building. During the manual flight, the autonomous fire detector shall warn the operator of the fire presence. Responsively, the operator can continue

with the inspection or can trigger an autonomous positioning with respect to the fire. Therefore the fire detection system provides an assisting technology capable of fast analysis and decision making. This analysis can contain information about the maximal temperature of a burning object, its 3D position and dimensions, and further data about the strength and spreading rate of the fire.

The task of the automatic aiming system is to find an efficient position suitable for the discharge of the capsule into the detected fire and precise autonomous navigation of the UAV, which has to comply with the physical characteristics of the capsule launcher and its ballistic curve. The capsule discharged into the fire shall not collide with any obstacle between the UAV and the fire. The main pillar of this application is hence the ability to detect and localize fires from onboard sensors in order to ensure an effective response to fast-spreading fires. The desired positioning of the UAV, with respect to the ballistic curve of the launcher and a fire, is depicted in Figure 2.1.
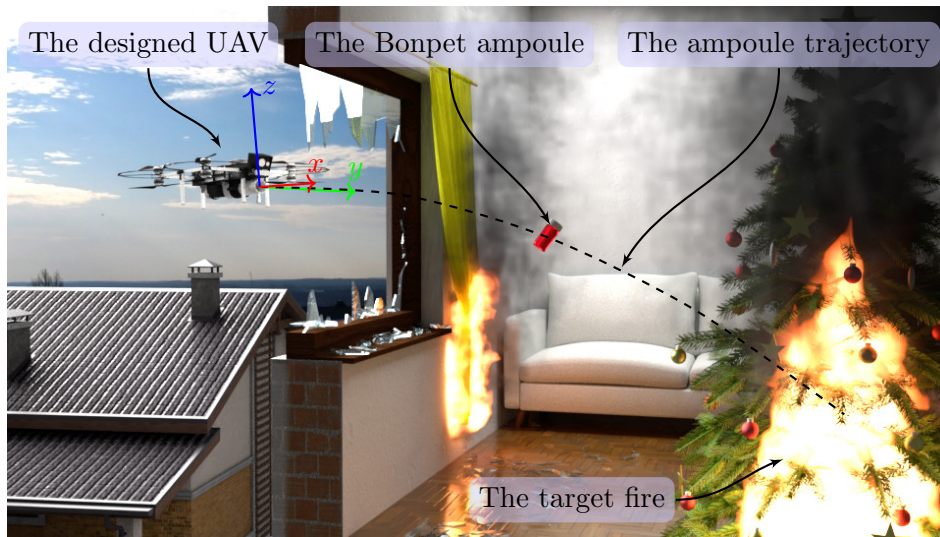
Figure 2.1: Visualization of the system application. Aim of the system is the autonomous detection and localization of fire, and an optimal discharge of the ampoule to the fire area.

2.2 UAV platform specifications

The primary requirement on the platform is the ability to carry an onboard launcher for discharging fire extinguishing capsules. This launcher mechanism is required to be positioned with a clear field for non-collision discharge, weigh less than 3 kg, and can produce significant dynamic recoil when discharging a capsule (see Section 3.4). The weight of the launcher has to be added to the model weight before the design of a drive subsystem, which consists of motors, propellers, and ESCs. This affects the choice of the number of motors and parameters of propellers. The design of the UAV platform is also significantly influenced by the physical dimensions of the launcher itself. Concisely, the launcher needs to be positioned such that the launched capsule does not collide with the UAV body. Discussion of the launcher characteristics is presented in detail in Section 3.4.

The discharge of the fire extinguishing capsule causes non-negligible kickback that disturbs the stabilization systems of the multicopter. For this reason, it is necessary to design the multicopter as stable as possible. Another way is to add a shock-absorber between the launcher and multicopter that could effectively decrease the influence of dynamic kickbacks. However, this work does not include this mechanism in order to keep the system as simple as possible to prove the concept of the application.

The stability of the drone is affected by many factors, namely regulator design, drive thrust-weight ratio, accuracy of sensors, the center of gravity location, and sensors and actuators position. The stability of the UAV in manual flight depends on motor thrust, autopilot, and operator experiences. The main factor influencing the UAV stability in autonomous flight is the performance of the UAV control. The designed system relies on the stabilization and control pipeline of UAVs developed in the MRS group. This system proved to be high performing, reliable, and robust in various real-world tasks and competitions [44–47]. It is therefore used in the presented application to control the UAV and to cope with the dynamic recoil of the launcher.

An important factor for physical flight is the drive thrust-weight ratio defined as a ratio between maximum total thrust (in kilogram) of all propellers and weight of the vehicle in the standard atmosphere on Earth [48]. The thrust-weight ratio is connected with maneuverability and affects the maximal possible acceleration of the UAV. Without a sufficient thrust-weight ratio, the UAV is not able to face all the stability disturbances. The geometric center of rotors situated in the center of gravity likewise increases the stability of the multicopter [49].

The application is designed such that a trained human operator controls the UAV from a safe distance far to the fire. After reaching the danger area, the operator can either manually trigger the fire extinguishing capsule launch or switch to an autonomous state where the UAV positions and fires the capsule on its own, using the data from onboard sensors. The ability to remotely control the UAV without clear operator-UAV visibility can be provided by first-person view (FPV) camera streaming video from the multicopter to the operator's screen. When the operator wants to explore an interior of the building he will probably lose visual contact with the UAV. In this case, the operator has full control over the vehicle and can navigate only via the streamed video feed. However, this scenario is not expected in this application, as the design expects the UAV to launch capsules from the exterior into the interior of a building. Flying indoors brings up several other challenges, such as complex onboard sensory setup, a capability of indoor-outdoor transit, or autonomous navigation in an indoor environment.

Autonomous detection of fire flames requires suitable sensory equipment, such as a thermal IR camera. To localize the detected fires, distance measurement sensors have to be equipped on board in order to estimate the 3D location of the fire with respect to the UAV. To process the onboard data and to reason about navigation and efficient launching of the capsule, a sufficient processing unit has to be likewise equipped onboard the UAV itself. All the necessary sensory equipment for the application increases the total weight of the UAV, which decreases the upper limit for the effective payload weight.

2.3 Operating environment characteristics

The environment around wildfire is extremely diverse and complex for the use of UAVs. The challenges that can appear in this environment and that can influence the mission have to be reflected in the system design itself. Hence, the difficulties that can be expected in operation with close proximity to sources of extensive heat are listed below. Accounting for these difficulties is necessary to consider various specific requirements to the multicopter:

- Quick temperature changes, which depend on the distance from the fire and the fire source itself.

- Dust and ash arising from airflow.

- Clouds of smoke influencing sensing capabilities of onboard sensors.

- Significant changes in light conditions caused by the fire.

- Dynamic obstacles like people, cars, or falling objects in close proximity to exteriors of buildings.

- Presence of the wind gust effect caused by high-temperature difference and wind outside the building.

- Possible presence of water drops in the flight area resulting from the nearby operation of firefighters or rain.

- Presence of difficult to detect obstacles like cables, rods, and similar objects close to exteriors of buildings.

Most of consumer electronics components have warranted functionality below temperature 80 °C. Special components, designed for automotive or aircraft industry, may typically operate even up to 120 °C, but the temperature near a fire may quickly rise over 300 °C [6,50], which makes most of the electronic components vulnerable.

The only solution to avoid the destruction of electronic components is to keep the UAV at a sufficient distance from the heat sources. However, a video stream from an onboard camera is not sufficient as the operator cannot estimate the air temperature just with an RGB view. Hence, an onboard thermometer must be equipped onboard and used to signalize the current temperature. This leads to the demand of an onboard thermometer with some signalization of approaching to a temperature limit. This limit should be set about 60 °C to 70 °C to provide enough time to escape with the UAV.

Ash and dust particles present in smoke clouds decrease the robustness of optical sensors, as small airborne particles can cause reflections of light beams used for time-of-flight or triangulation determination of distance in laser-based sensors. That causes fake detection of objects near the UAV disturbing navigation and stabilization of the UAV. These particles also cause diffusion of the light so distant objects may not be detected because the intensity of the reflected light beam is lost.

Further, the large particles in combination with dynamic changes of light conditions will affect the quality of video streamed from the UAV to the human operator. Impaired video

quality and the presence of hard to recognize objects make control of the UAV very difficult. This requires the UAV to be equipped with a special safety mechanism that can prevent collisions between an obstacle and a propeller blade. This safety border can also prevent from breaking the propeller in collision with an undetected object. To avoid sensor discrepancy in these environments, the system has to increase robustness by the inclusion of appropriate sensors and hardware protection. The most reliable sensor in this application is ultrasonic rangefinder in combination with hardware protection.

Wind gust effect can cause a collision with a static obstacle like a wall, window, or door frame. This issue should solve the safety mechanism recommended above. Wind gust effect can also cause a big error in the stabilization of the position of the UAV. To overcome this issue, a GPS receiver needs to be employed in order to stabilize the UAV during the mission. There is no suitable way to determine the position of drone inside the building because of this environment. Therefore autonomous operation is not possible inside a burning building.

To protect the onboard electronics from water drops and humidity, the electronics are required to be covered with sufficient protection. This cover should protect the main electrical part, but can't impede motors and propellers for obvious reasons. However, typically used brushless DC motors for UAV systems are certified for use in rain, e.g., *T-Motor*'s *U* series has IP33 certification [51], *V* series has even IP45 certification [52].

The size of the UAV platform has a big effect on the navigational capabilities of the UAV through the environment. Smaller UAVs can more easily navigate safely through narrow corridors or even through windows and doors, but smaller propellers produce smaller thrust. Therefore the size has to compromise between the weight and the maneuverability. The UAV platform in the proposed system is designed to carry a launcher that weights up to 3 kg, thus the UAV requires larger propellers in a feasible configuration in order to produce enough thrust.

2.4 MRS system for autonomous UAV control

This thesis takes as a baseline the UAV stabilization and control pipeline of the MRS group at FEE CTU. This pipeline is part of a complex open-source system developed in the MRS group, publicly available at `https://github.com/ctu-mrs/`. This system is based on Robotics Operating System (ROS) [53]. ROS provides a framework for communication and data transfer between processes (nodes) running on one or more computers. The inter-node communication is based on sending a special message over TCP-IP protocol. These messages are distributed to topics and services according to the message purpose. Messages belonging to one topic can be received and transmitted by multiple nodes. Services are suited for interaction between two nodes. A service contains a request message and a response message.

The MRS system also employs the Gazebo robotic simulator [54] used for simulation of UAVs, together with the onboard running stabilization and control systems. This simulator is commonly used in the field of robotics for its realistic physics, easy to use interface, and sensors and actuators implementation of their communication interface. Furthermore, the simulation employs the same source code and hence the interface as the real worlds allowing for easy integration of the developed algorithms onto real hardware. To perform simulated experiments of the proposed design, a Gazebo plugin capable to simulate the thermal camera

was prepared. This plugin decodes the temperature information (encoded in the object texture color) and provides it in the same format as the used thermal camera.

All the simulation scenarios presented in this thesis take part in the simulated world prepared for the MBZIRC fire challange [55]. This simulation scenario contains ground fires as well as fires on and inside a high-rise building (see Figure 2.2).
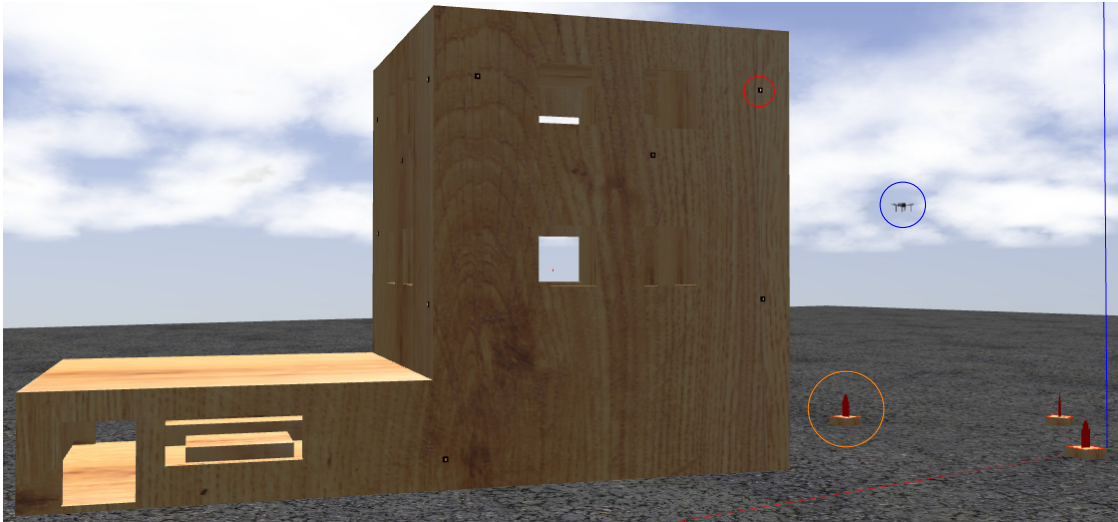
Figure 2.2: Visualization of the simulated world containing a tall building with indoor and outdoor fires (red), ground fires (orange), and the UAV (blue) detecting and localizing the fires in real time.

The stabilization and control pipeline of UAVs [56] provides robust stabilization and localization system stabilization, which employs a localization source. Throughout this thesis, this localization source is a GPS receiver. The system takes care of state estimation and feedback control of the UAV to provide minimal state error. The desired state is given to the reference tracker which prepares a desired reference setpoint or a trajectory for a UAV controller. The system can be accessed as a black box by easy-to-use interface that allows quick and safe UAV positioning and navigation.

Chapter 3: Hardware Design

Contents

The design consists of the construction frame, the drive unit, and the electronic equipment. The construction frame creates a solid platform for the mounting of all other components. The drive provides the necessary thrust to fly and power for all electronics. The electronic equipment consists of sensors and computational unit that is required to stabilize the UAV and detect and localize unknown fires. The design of the entire hardware and software system has to respect mutual mechanical and electronic compatibility between all the components which are discussed in detail in this chapter.

3.1 Frame

There are many kinds of frames different in shape and motor placement. The most common rotor configuration is the quad-rotor with 4 rotors placed on extreme points of a square base. Due to high weight payload, only four motors do not provide sufficient thrust. Hence it is necessary to use more rotors. To minimize the total dimensions of the platform, their placement must be efficiently chosen. To do so, the coaxial rotor configuration is employed to obtain smaller sized UAV with an increased number of motors, hence the ability to produce larger thrust. The use of coaxial rotors allows us to use double the motors on UAV with the same dimensions as in four-rotor configuration. Coaxial rotor consists of two motors and propellers rotating about the same axis but contra-rotary directions, as shown in Figure 3.1. A coaxial motor has reduced efficiency up to approximately 14% in contrast to the same two motors placed standalone [57]. However this loose of thrust is balanced by lighter frame construction. Hence, coaxial rotor configuration is ideal for use on platforms requiring minimalist dimensions and maximalist takeoff weight capacity, such as required in our application. The frame configuration of the designed UAV is based on octocopter X8, which is shown in Figure 3.2.

The main purpose of the frame is to provide a connected platform to mount motors and base components on. The frame can, in general, have tree shapes, namely rectangular, H-shape, or X-shape. H-shape or X-shape provides direct connection only between the base
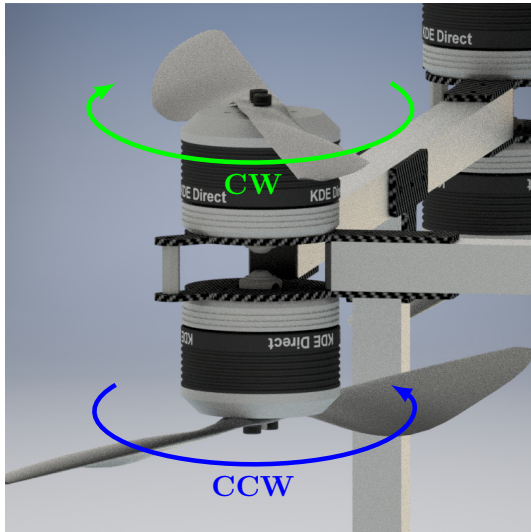
Figure 3.1: Coaxial rotor principle.
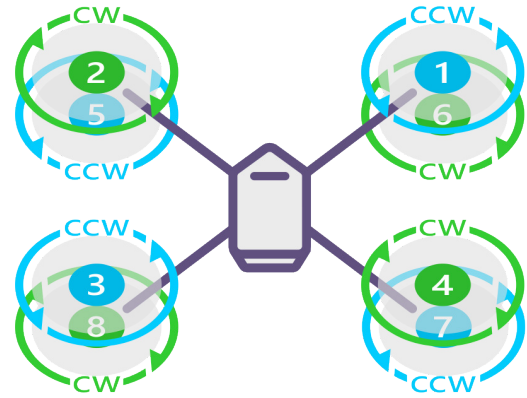
OCTO QUAD X8

Figure 3.2: Selected rotor placement in X8 configuration [1].

component and one coaxial rotor, which induces the risk of arm twists during higher mechanical stresses. On the other hand, the rectangular frame connects all rotors in the orthogonal axes, which improves the stiffness of the frame, hence reduces the risk of the construction deformation. This is why the rectangular frame is suitable for this UAV, which needs to be lightweight but strong enough to cope with all the inertial forces and handle motors momentum.
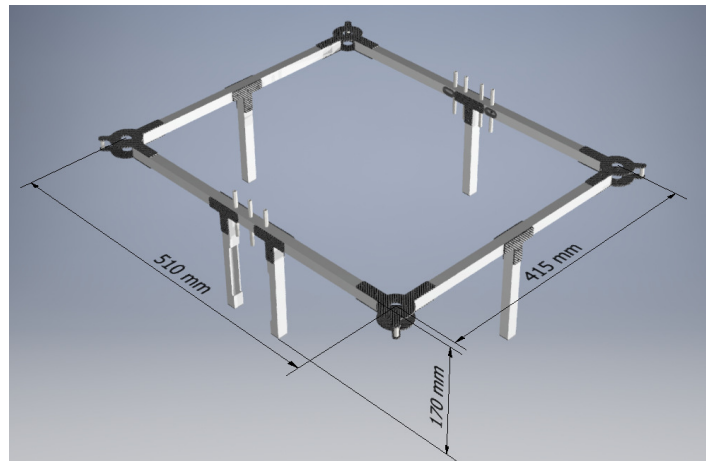
Figure 3.3: Frame connecting motors and base component.

The proposed frame design consists of a core part holding motors and a base component equipped with electronics and sensors. Landing gear is also integrated into the core component which is shown in Figure 3.3. This core component is made from aluminum squared frame tubes due to its lightweight and stiffness properties. These aluminum tubes are connected by carbon fiber composite, which is a modern material in aerospace due to its great ratio among weight and stiffness.

3.1.1 Base component

The base component provides a mounting platform to equip the launcher, computer, batteries, sensors, power distribution, and other electronics on. It aspires to be as light as possible and robust enough to face dynamic tension caused by inertial forces coming from quick maneuvers. For this, the carbon fibre is ideal for its density of $1.81\,\mathrm{g\,cm^{-3}}$ [58]. Fabrication of complex 3D shapes from carbon fiber composite is rather expensive and requires advanced technological equipment. For this reason, the entire presented design is based on 2D carbon parts, which are milled from simple carbon fiber composite plates of $2\,\mathrm{mm}$ width.

The base component consists of two vertically-stacked layers. The flat bottom layer is designed for mounting of the fire extinguishing ampoule launcher, while the top layer is designed for mounting of computer and other electronics. These layers are likewise milled out from carbon plates.

To improve the stability of the dynamically unstable UAV system, the center of gravity of the design is matched with its geometric center. The battery pack, which is the second heaviest component after the ampoule launcher, is positioned into the geometric center of rotors between the top and bottom layers. The space within the base component is further used to suit ESCs and the power distribution for all the onboard electronics. The base component is likewise stiffened up with vertical reinforcements in the form of side panels. The battery is held in by 3D printed closable doors. The model of the entire base component is shown in Figure 3.4.
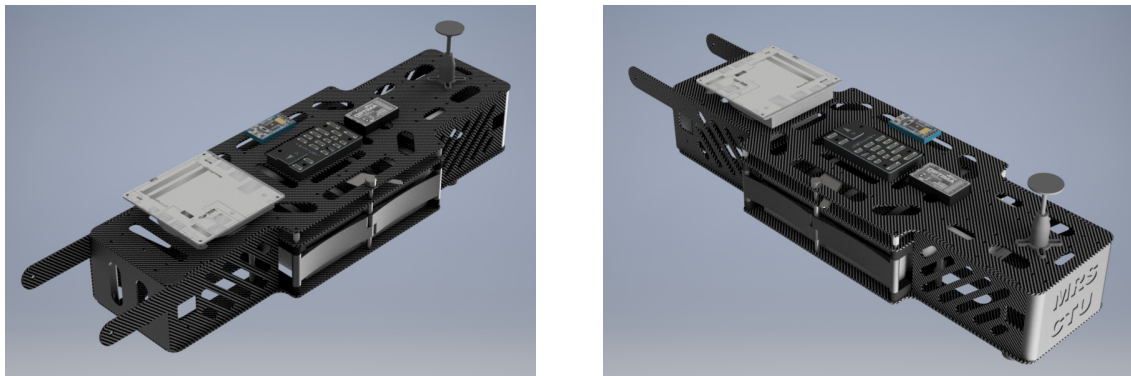
Figure 3.4: Visualization of the entire base component with autopilot and onboard computer.

The top layer is used for the mounting of sensory equipment, namely the thermal, FPV, and depth camera. These cameras are mounted to the front of the base component on the external mount, which allows for rotation of the cameras around their horizontal axis. Figure 3.5 shows the CAD drawings of this mounting mechanism.

3.1.2 Landing gear

It is common to use some kind of slant landing gear connected to the bottom part of the platform in combination with coaxial rotors. This is, however, a quite unstable option, as it adds tension to the center part of the platform during landing and reduces space under the platform necessary for the launcher, as shown in Figure 3.7. A more suitable solution spreads
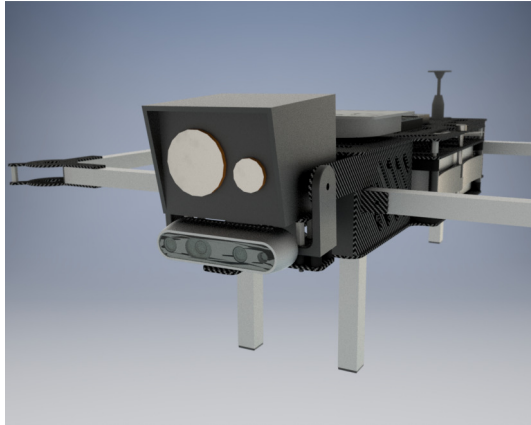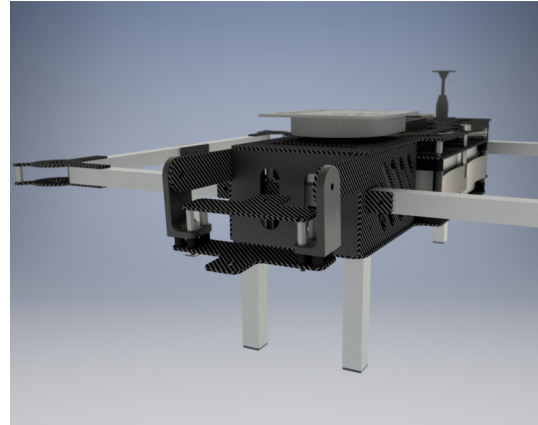
(a) A visualization of the onboard cameras.   (b) A figure of the mounting mechanism.

Figure 3.5: A visualization of the onboard cameras (a) and their mounting mechanism with rotational horizontal axis (b).

out the landing gear throughout the entire frame construction, which distributes the mechanical load all around the robust construction. The proposed design, visualized in Figure 3.6, places these vertical legs effectively around the entire bottom layout to reduce mechanical stress on the construction, which results in sufficient protection of onboard electronics during takeoff and landing.
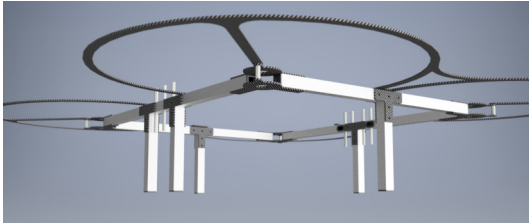
Figure 3.6: Landing gear connected to the core component.
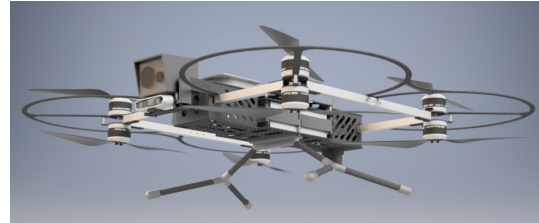
Figure 3.7: Landing gear connected to the base component.

3.1.3   Safety mechanism

Safety mechanism can prevent propeller destruction in case of a mild horizontal collision with an obstacle caused by the dynamic kickback arising from the discharge of fire extinguishing capsule. For this reason, a horizontal propeller guard system extends the construction around propellers to provide the low-level hardware protection from mild collisions, as shown in Figure 3.8. This system consists of two parts made from carbon plates connected directly to the UAV's frame. The constructed prototype, shown in Figure 3.15, is not equipped with this collision handling system as the initial experiments did not require flying in close proximity of obstacles. If required, the designed platform can be easily mounted with these propeller guards.
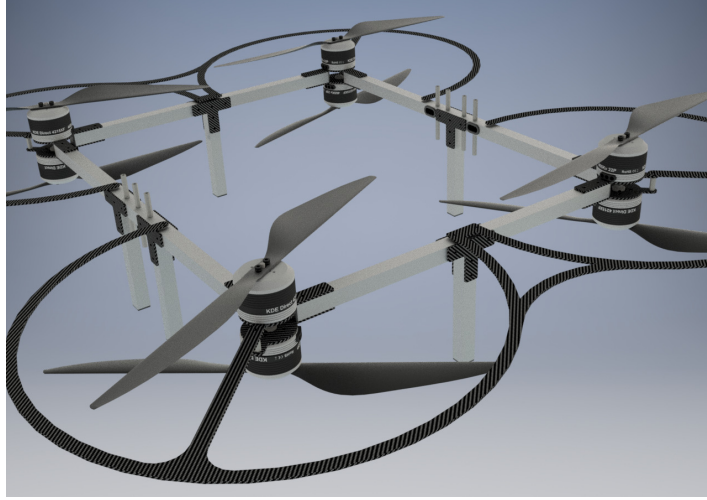
Figure 3.8: Horizontal safety mechanism.

3.2 Drive

Drive consists of a battery, electronic speed controllers (ESC), motors, and propellers. The choice of these components affects the flight characteristic of the UAV, namely weight, size, generated thrust, and flight time. As the commercial market is extremely huge, the choice of components must likewise account for the mutual compatibility between motor propellers, motors, and battery voltage.

There is an online tool eCalc [2] suitable for finding optional drive parts and its parameters. This tool provides calculation of the flight characteristic according to selected drive component and UAV weight. The UAV weight was estimated by creating a 3D model containing all components listed bellow in Table 3.1 with correct weight and density set-up. This model was parameterized by the size of propellers and motors to allow quick weight re-estimation after components change while finding its optimal combination.

Selected components and their parameters are summarized in Table 3.1 and further described in detail in Section 3.2.1. These components compromise between UAV size, high-weight payload, and ensure mutual compatibility. Flight characteristics of the UAV with this designed drive are described in Figure 3.9.

3.2.1 Drive components

Motor

Brushless direct current motors are commonly used in UAV systems. The brushless motor is determined by several key parameters, namely its power limit, resistance, weight, Kv, current, and voltage limit. Another limiting factor is the motor geometry dimensions and specifications of propeller compatibility. Motors with a self-tightening propeller mount can rotate only in one direction specified by the manufacturer to ensure propeller attachment.

Segment	Component	Specifications	Weight [g]
Drive	Motors	KDE4215XF-465	8×195
	Electronic Speed Controller	Flycolor X-Cross	8×6.3
	Propellers	T-Motor Prop 12×5	8×21
	Accumulator	Tattu 6S LiPo	2×1105
Frame	Base	Carbon, aluminum, and 3D printed parts	755
	Core with landing gear	Carbon and aluminum parts	711
	Cameras holder	Carbon and 3D printed parts	51
Electronics	Central processing unit	Intel NUC8i5	220
	Autopilot	Pixhawk 4	15.8
	Sensors data acquisition board	Drone Peripheral Hub	180
	Power board	Self made PCB	63
	Radio control receiver	Optima 8, 2.4 GHz	22
Sensors	Optical rangefinders	Garmin Lidar Lite v3	22
	Front-facing depth camera	RealSense D435	72
	Thermal camera	Wiris Pro 640	450
	GPS/GLONASS receiver	PixHawk ublox Neo-M8N	23
Payload	Extinguishing capsule launcher	Launcher	2448
	Launcher holder	3D printed parts	367
	Extinguishing capsule	Bonpet Grenade	557
			9945, 2

Table 3.1: List of the used components with their weight.

Not all of the manufacturers offer bidirectional motors. Hence not all commercially available motors can be used.

The main parameters of brushless motors design are the power limit, the motor velocity constant K_v, motor resistance, and its weight. The power limit defines the maximum power in Watts provided by the motor. K_v comes from a simple electrical motor model described in [59]. This model defines electrical motor as a serial connection of a resistor with the same resistance as the motor and back electromotive voltage source, where the amplitude of back electromotive voltage V_{peak} depends on the motor speed ω. K_v is the number of motor revolutions per minute divided by back electromotive voltage (revolution per minute per volt)

$$K_v = \frac{\omega}{V_{peak}}. \tag{3.1}$$

Since the motor resistance is typically small (e.g., $52\,\mathrm{m\Omega}$), it is a good approximation that the speed of an unloaded motor equals K_v multiplied by the motor input voltage.

Concerning our UAV specifications, the employed brushless motor is KDE4215XF-465 with characteristics of bidirectionality, 456 Kv, 1375 W power limit, and a universal propeller

General | Model Weight: | 10000 g incl. Drive | 352.7 oz | # of Rotors: 8 / coaxial | Frame Size: 600 mm / 23.62 inch | FCU Tilt Limit: no limit | Field Elevation: 500 m.ASL / 1640 ft.ASL | Air Temperature: 25 °C / 77 °F | Pressure (QNH): 1013 hPa / 29.91 inHg

Battery Cell | Type (Cont. / max. C) - charge state: LiPo 8000mAh - 20/30C - normal | Configuration: 6 S 2 P | Cell Capacity: 8000 mAh / 16000 mAh total | max. discharge: 85% | Resistance: 0.0028 Ohm | Voltage: 3.7 V | C-Rate: 20 C cont. / 30 C max | Weight: 189 g / 6.7 oz

Controller | Type: max 40A | Current: 40 A cont. / 40 A max | Resistance: 0.006 Ohm | Weight: 50 g / 1.8 oz | Accessories | Current drain: 3 A | Weight: 0 g / 0 oz

Motor | Manufacturer - Type (Kv) - Cooling: KDEDirect - KDE4215XF-465 (465) - good, search... | KV (w/o torque): 465 rpm/V, Prop-Kv-Wizard | no-load Current: 0.7 A @ 10 V | Limit (up to 15s): 1375 W | Resistance: 0.052 Ohm | Case Length: 36 mm / 1.42 inch | # mag. Poles: 22 | Weight: 195 g / 6.9 oz

Propeller | Type - yoke twist: Aeronaut CamCarbon - 0° | Diameter: 15 inch / 381 mm | Pitch: 5 inch / 127 mm | # Blades: 2 | PConst / TConst: 1.07 / 0.99 | Gear Ratio: 1 : 1 | calculate

Load: 16.78 | Hover Flight Time: 9.2 | electric Power: 655.1 | est. Temperature: 55 | Thrust-Weight: 2 | specific Thrust: 5.48 | Configuration

Remarks:

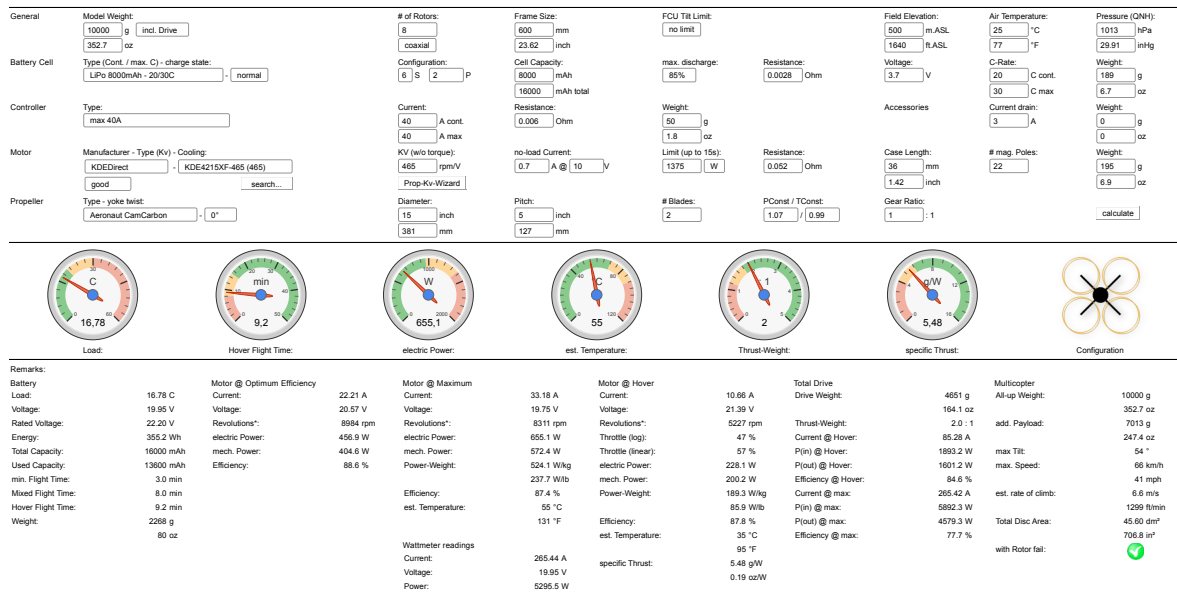| Battery		Motor @ Optimum Efficiency		Motor @ Maximum		Motor @ Hover		Total Drive		Multicopter	
Load:	16.78 C	Current:	22.21 A	Current:	33.18 A	Current:	10.66 A	Drive Weight:	4651 g	All-up Weight:	10000 g
Voltage:	19.95 V	Voltage:	20.57 V	Voltage:	19.75 V	Voltage:	21.39 V		164.1 oz		352.7 oz
Rated Voltage:	22.20 V	Revolutions*:	8984 rpm	Revolutions*:	8311 rpm	Revolutions*:	5227 rpm	Thrust-Weight:	2.0 : 1	add. Payload:	7013 g
Energy:	355.2 Wh	electric Power:	456.9 W	electric Power:	655.1 W	Throttle (log):	47 %	Current @ Hover:	85.28 A		247.4 oz
Total Capacity:	16000 mAh	mech. Power:	404.6 W	mech. Power:	572.4 W	Throttle (linear):	57 %	P(in) @ Hover:	1893.2 W	max Tilt:	54 °
Used Capacity:	13600 mAh	Efficiency:	88.6 %	Power-Weight:	524.1 W/kg	electric Power:	228.1 W	P(out) @ Hover:	1601.2 W	max. Speed:	66 km/h
min. Flight Time:	3.0 min				237.7 W/lb	mech. Power:	200.2 W	Efficiency @ Hover:	84.6 %		41 mph
Mixed Flight Time:	8.0 min			Efficiency:	87.4 %	Power-Weight:	189.3 W/kg	Current @ max:	265.42 A	est. rate of climb:	6.6 m/s
Hover Flight Time:	9.2 min			est. Temperature:	55 °C		85.9 W/lb	P(in) @ max:	5892.3 W		1299 ft/min
Weight:	2268 g				131 °F	Efficiency:	87.8 %	P(out) @ max:	4579.3 W	Total Disc Area:	45.60 dm²
	80 oz					est. Temperature:	35 °C	Efficiency @ max:	77.7 %		706.8 in²
				Wattmeter readings			95 °F			with Rotor fail:	✅
				Current:	265.44 A	specific Thrust:	5.48 g/W				
				Voltage:	19.95 V		0.19 oz/W				
				Power:	5295.5 W						

Figure 3.9: UAV design characteristic using the eCalc web tool [2].

mount [60]. However, this motor type does not provide any water resistance certification, which diminishes its use in rainy conditions. If the water resistance certification is required for real-world applications, the selected motors can be easily upgraded with a suitable type.

Propeller

A propeller is defined by its diameter and pitch. Pitch defines the propeller's vertical shift after one revolution in a solid environment. Rotation of a propeller generates lift. This principle is well-known in the field of aeronautics and it is henceforth referred to as thrust in our case. Concisely, lift is generated from different air pressure on the propeller sides and can be influenced by the shape of a propeller, as well as its pitch and length.

Carbon fiber composite propellers with 15 inches length and 5 inches pitch were selected for the expected application requiring 10 kg for takeoff according to Table 3.1. According to the eCalc online tool, the combination of these propellers with the selected motors and their configuration provides 20 kg of thrust with maximum power at 655.1 W. This makes them sufficient for the presented application. The selected propellers are also suitable for working below temperature 65 °C and can't be used in an environment containing corrosive gases [61]. Although the manufacturer specifications do not mention any information about deployment in rainy or humid conditions, their functionality is assumed to be intact in these environments due to the employed construction material (carbon fiber).

Battery

The battery pack provides a power supply for all electronic components on the UAV. It powers the motors, ESC, onboard computer, sensors, and even the launcher. Its main parameters are capacity, weight, maximum discharging rate, and the number of parallel and

serial cells. The number of cells in series designates battery output voltage that should be accepted by ESCs and motors. The capacity of the battery determines how much energy can be stored in the battery and the maximum discharging rate denotes maximum current that can be drawn from the battery.

In our design, the battery consists of two parallel accumulators, each containing six LiPo cells in series. This configuration provides maximum continuous current 400 A with nominal voltage 22.2 V. The total capacity reaches 16 Ah with a total weight of 2338 g.

Electronic Speed Controller

Electronic speed controllers serve as a translation layer between the autopilot and the motors. They translate the signal from autopilot to three-phase high-current power input to the motors. Their key parameters are continuous current, maximum peak current, input voltage range, and a supported communication protocol. The developed design employs ESCs with pulse width modulated (PWM) control signal input and characteristics of 35 A continuous current on a battery with a nominal voltage of 22.2 V.

3.3   Electronics

The onboard electronics consist of sensory equipment, an autopilot, a processing unit, and the drive system described in Section 3.2.1. The previously undiscussed components are described in detail in this section.

3.3.1   Autopilot

An autopilot provides stabilization and low-level control of the UAV. Its main function lays in the accurate production of tilt and appropriate thrust with respect to the desired motion. In principle, the autopilot designates a specific value of thrust to each individual motor and sends the command to the particular ESC. With inner sensors, the autopilot can stabilize the dynamical system of mid-flight UAV. The autopilots are equipped at least with an accelerometer and a gyroscope. Although these sensors suffice for airborne stabilization of UAV, they are, in modern devices, supplied by barometers and magnetometers. A reliable autopilot also introduces a sensor redundancy by containing more than one of these sensors to improve robustness towards a single point of sensor failure.

The presented design includes PixHawk 4 [62] autopilot based on the PX4 stack, as required by the system for the stabilization of a UAV developed by the Multi-Robot Systems group. This embedded device is equipped with an Inertial Measurement Unit (IMU), plenty of peripherals, integrated vibration isolation, and software support. The inner IMU is thermally stabilized and contains a barometer for global altitude measurements, a magnetometer for global azimuth, 3 accelerometers to measure linear acceleration, and a gyroscope to measure the angular rate.

3.3.2 Additional equipment

Sensors included in the autopilot provide only measurements of acceleration, which can be integrated into an estimation of velocity and position. Because of the non-zero measurement error of the sensors, this methodology is prone to error and time-based drift, and hence can't be relied on for long-term stabilization and navigation. Therefore other suitable sensors are required not just for airborne stabilization and global positioning of the UAV but also for perception of the environment (e.g., fire detection and localization).This equipment is described further in this section.

Thermal camera

A thermal camera provides a stream of images describing the temperature of the seen object. These images come from non-contact temperature measurements. The theory and challenges of contactless temperature measurement are described thoroughly in Section 4.1.1. This section also shows the use of temperature measurement in fire detection tasks, which proves to be more robust than sole RGB images due to the contrast between fire and ambient temperatures.

The proposed design uses the Wiris Pro 640 thermal camera developed by Workswell [63]. The camera specifications are high-resolution, internal image stabilization, high range of measurement, high thermal sensitivity, and durable design optimized for usage on UAVs. This camera also provides an RGB image stream that can be streamed to the ground operator, which removes the need for an additional FPV camera. The transport of the image streams uses real time transport protocol, which can be easily decoded by a variety of software. The video stream opencv package [64] is used to decode these streams to ROS image topics. The camera also provides information about maximal and minimal temperature in the image through TCP protocol. This information is necessary because the range of the received image is scaled according to the minimal and maximal measured temperature. A simple ROS package was implemented to obtain this information from the camera and publish it as a topic into the ROS network.

Depth camera

A depth camera estimates 3D depth in its defined field-of-view and outputs a 2D image with the distance encoded in the pixel values. Although there are several methods for estimation of the image depth, the most common methodology uses a stereo camera, whose known baseline width is used to estimate the 3D position of common image features.

In the proposed design, a depth camera is used to estimate the 3D position of a detected fire. Although a point-distance rangefinder could be used for measuring the distance from the detected fire, there remains a need for an accurate positioning of the optic beam into the detection. Therefore, a depth camera is a better-suited sensor for the presented application due to its field of view.

In the proposed design, Intel Realsense D435i [65] depth camera is used due to it being lightweight, well-tested by the robotic community, and easy to integrate into existing systems. This camera uses two infra-red cameras to find projected light markers and estimates their depth.

Thermometer

A passive thermometer is necessary to warn the operator if the temperature of the UAV raises to safety limit configured in such a way that all onboard electronics remain fully functional. For this purpose, the presented design includes an LM35 thermometer with voltage output linearly corresponding with temperature from range $-55\,°C$ to $150\,°C$.

Laser range finder

A point-distance laser rangefinder serves as an altimeter by measuring the distance from the ground. This measurement is then used for aerial stabilization of the UAV. The presented design uses Garmin LIDAR-Lite v3 laser rangefinder, which is lightweight and has specifications of $40\,m$ range, up to $1\,cm$ resolution and $\pm\,2.5\,cm$ accuracy.

GPS

GPS receiver is also necessary for absolute position stabilization and control. PixHawk ublox Neo-M8N GPS/GLONASS receiver with integrated magnetometer IST8310 [66] is used for this application due to its accuracy of $2.5\,m$ and compatibility with the selected autopilot.

3.3.3   Computation unit

An onboard computational unit is necessary for stabilization and control, mission control, sensor data processing, trajectory planning, and fire detection and localization. The presented design employs Intel NUC 8i5BEK with a 4-core processor of $2.3\,GHz$ frequency. This onboard computer specifications are: compact design, sufficient number of peripherals, input voltage of $12\,V$ to $19\,V$ and $220\,g$ weight. Based on the experimental testing, all the aforementioned subsystems of the UAV do not require more than $50\,\%$ of the total processing power of this particular computational unit.

3.3.4   Electronics connection

Each onboard electronics component requires a power supply and a communication interface. The brain of the UAV is the onboard computer whose purpose is to control the whole UAV and reflect its state. Therefore the computer must communicate with all the sensors and actuators but not all the sensors and actuators can be connected directly to the computer due to different communication standards. Therefore lower-level devices are connected through so-called Drone Peripheral Hub that is described below in this section. Other components that need to be driven in real-time are connected straight to the autopilot for its real-time software support.

Main power delivery is ensured by a designed power circuit board that provides power for ESCs, the thermal camera, and Drone Peripheral Hub that redistribute power for sensors, the computer, and autopilot. Power and signals connections are shown in Figure 3.10.
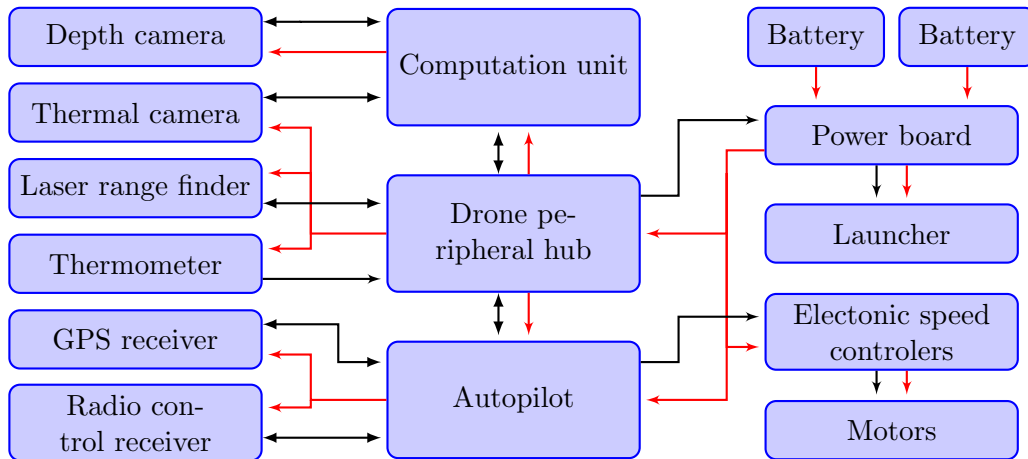
Figure 3.10: High-level connection diagram. Red is power lines and black signal lines.

Drone Peripheral Hub

The master is the onboard computer that should be able to communicate with all other components and control them. For this purpose, Drone Peripheral Hub was designed by the MRS group. Drone Peripheral Hub provides a bridge between universal serial bus (USB) and other communication standards, for example, I2C, UART, SWD. It also provide USB hub, analog inputs, controlled 12 V and 5 V power output, digital input-output ports, 12 V and 5 V power supply for other devices, and special power port for autopilot.

Drone Peripheral Hub is used for connection of the launcher, Garmin LIDAR-Lite v3 range-finder, thermometer, and autopilot to the onboard computer. It is also used as the computer and autopilot power supply.

Power board

A power printed circuit board was developed to provide power for all the electronics components. This board provides the ability for parallel battery connection and distribution of power for ESC, Drone Peripheral Hub, and thermal camera. It also provides a redundant power source for autopilot. In case of failure, the UAV can fly only with working autopilot and one broken motor, propeller, or ESC. Therefore secondary power supply for autopilot is included.

The designed board layout is shown in Figure 3.11. The board consists of two parts connected by wire to save space and material because ESCs are distributed into two groups. Each part provides power for its ESC group. The bigger part also provides power for the remaining components. This part also contains diodes to protect the accumulator from charging one from the other. There is also 5 V voltage regulator 7805cv that can provide 1.5 A for the autopilot like secondary power source. This part also contains a relay to connect the launcher input to the battery for triggering the discharge of the fire extinguishing capsule. To avoid heating or destruction of supply traces that are powering all the electronic components, this was reinforced by additional copper wire like it is in Figure 3.12.
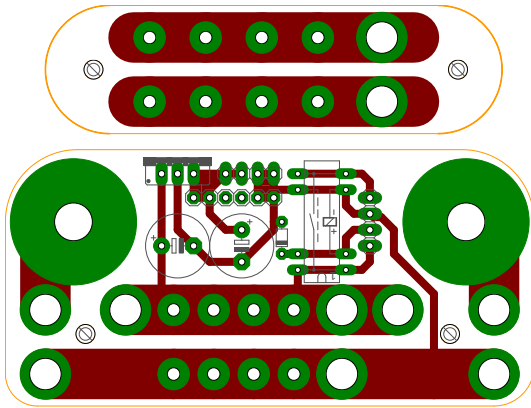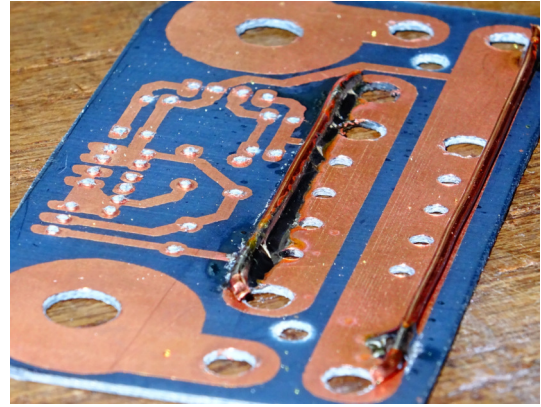
Figure 3.11: Power printed circuit board layout.

Figure 3.12: Trace reinforced by additional wire.

3.4 Launcher

The ampule launcher provided by an external supplier is able to discharge the ampoule weighing $0.557\,\mathrm{kg}$ to distance about $10\,\mathrm{m}$. The launcher loaded with the ampoule weights $3.005\,\mathrm{kg}$. This launcher is powered by compressed gas coming from single-use $16\,\mathrm{g}$ carbon dioxide cartridge. The gas is closed in the first chamber by a solenoid valve, after activation of the solenoid valve the gas flows from the first chamber to the launcher muzzle and the pressure of the gas forces out the ampoule. The solenoid valve is activated by $24\,\mathrm{V}$ voltage input. The model of the launcher is shown in Figure 3.13.
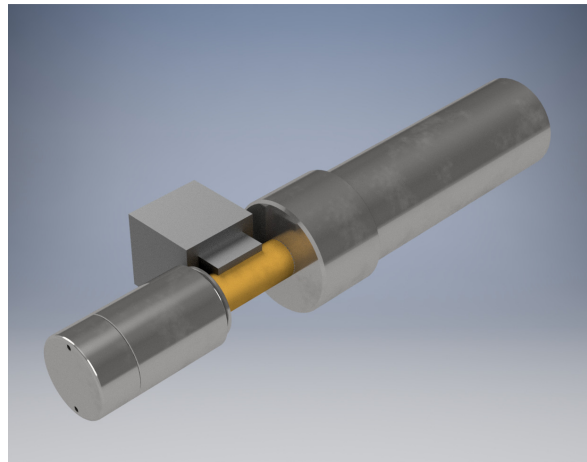

Figure 3.13: 3D render of the launcher capable of discharging a $0.557\,\mathrm{kg}$ fire extinguinshing ampoule as far as $10\,\mathrm{m}$.

3.5 Final multicopter

Final UAV design is shown in Figure 3.14 and its realized prototype is shown in Figure 3.15. The final prototype weights $9934\,\mathrm{g}$ and has dimensions of $912\,\mathrm{mm}$ by $817\,\mathrm{mm}$. The

designed UAV is capable to fly and horizontally exhaust onboard payload with 557 g weight.
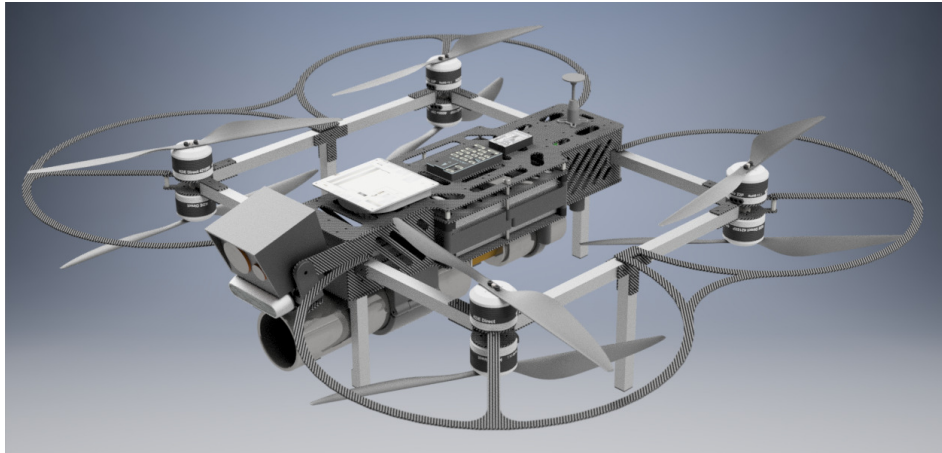

Figure 3.14: Final design of the entire multicopter.

This UAV carries all components needed for fire detection, localization, and automatic positioning in order to launch the fire extinguishing capsules into a detected fire. It also supports human-operated flight to manually navigate the UAV towards the fire. For this purpose FPV system was recommended but it is not mounted to the realized prototype because clear operator-UAV visibility is ensured while testing, therefore it is not necessary on the prototype but can be added after.

(a) Stationary photo with mounted launcher.

(b) Airborne photo of the entire UAV.

(c) Airborne photo during autonomous test flight.

(d) Airborne photo during a manoeuvre.

(e) Airborne photo of the complete system.

(f) Airborne photo without the launcher.

Figure 3.15: Realized prototype of the UAV.

Chapter 4: Fire Detection & Localization

Contents

The purpose of the designed UAV system is to help an operator in the detection and localization of unknown fire sources, followed by their extinguishment. The location of fires is assumed to vary from interiors to exteriors — the fire sources may exist on walls, on roofs, or inside a building behind a broken or an opened window, or behind a cracked wall. The proposed design focuses on extinguishing fire sources inside a building as the used extinguishing ampoule [4] is in principle more efficient in bounded space rather than in an exterior. This section discusses a designed strategy and challenges of the detection and localization of these sources solely from onboard sensors. The discussion is then extended by an autonomous relative positioning of the UAV concerning the localized object of interest — a fire.

4.1 Fire detection

The task of the fire detection system is to classify an object in image data as a fire if it is present in the data. This object is represented by a set of pixels with a shared attribute. In thermal imaging, this attribute is the temperature. The proposed fire detection method relies on high contrast between a fire source and ambient temperature, which is typical in thermal imaging. Although the detection of a hot object in thermal images is easier than in RGB images, thermal imaging brings several challenges arising from non-contact temperature measuring. This section discusses the methodology of non-contact temperature measurement, introduces an example of produced thermal images by the employed thermal camera, and presents an efficient algorithm for fire detection in these images.

4.1.1 Non-contact temperature measurement

Non-contact temperature measurement [67] is based on measuring the energy of electromagnetic (EM) radiation emitted in the infra-red (IR) part of the EM spectrum. The EM radiation is continuously produced by every object whose temperature is higher than $0\,\mathrm{K}$. The emitted radiation quantity is described by radiant exitance M_e $[\mathrm{W\,m^{-2}}]$, which represents the EM energy flux emitted by the unit surface of the object. Radiant exitance of the object

depends on its temperature T [K] and emissivity ε [-]. The total radiant exitance emitted by the object is given by Stefan–Boltzmann law

$$M_e = \sigma \varepsilon T^4, \tag{4.1}$$

where σ [Wm^{-2}K^{-4}] is the Stefan–Boltzmann constant. Radiant exitance spectral distribution called spectral exitance follow the Planck's law

$$\frac{\partial M_e}{\partial \nu} = \frac{2h\nu^3}{c^2} \frac{1}{e^{\frac{h\nu}{k_b T}} - 1}, \tag{4.2}$$

where ν [Hz] is the EM radiation frequency, k_B [JK^{-1}] is the Boltzmann constant, h [J s] is the Planck constant, and c [m s^{-1}] is the speed of light. The frequency of the maximal radiant exitance ν_{peak} [Hz] can be obtained from the Wien's displacement law

$$\nu_{peak} = \frac{cT}{b}, \tag{4.3}$$

where b [m K] is the Wien's displacement constant.

The emissivity describes how well the object surface emits the EM radiation in comparison with an ideally emitting object called a black body. In contrast to real objects that absorb only part of the irradiation, the black body absorbs all of the incident EM radiation. The emissivity is defined as

$$\varepsilon = \frac{M_e}{M_e^0}, \tag{4.4}$$

where M_e [W m^{-2}] is radiant exitance of the surface and M_e^0 [W m^{-2}] is radiant exitance of black body at the same temperature as that surface. The black body has emissivity $\varepsilon = 1$, while polished metals can have emissivity lower than 0.1. Differences in surface emissivity yield significant errors to contactless temperature measurement. Therefore emissivity of the measured object has to be calibrated and set in the thermal camera. However, this error is negligible in comparison with the contrast between fire and ambient temperature.

Contactless thermometers measure irradiance E_e [W m^{-2}], which is the received EM energy flux per unit area. The irradiance is measured indirectly by measuring the temperature change of a minimalistic thermometer caused by the incoming energy in the EM form of the irradiance. Between the contactless thermometer and a measured object is an ambient environment causing a dissipation of the radiation energy emitted by the measured object. This dissipation is caused by the EM radiation collision with gas molecules and solid objects. These obstacles absorb and reflect the radiation energy. The amount of absorbed and reflected radiation in the obstacle depends on the passing radiation frequency and the obstacle material. For example, water vapor absorbs all radiation with wavelength ranging from 5.5 µm to 7.5 µm [68] and low-emissivity glass absorbs and reflects almost all radiation with a wavelength higher than 2 µm [69]. This is also illustrated in Figure 4.1, showing a comparison between the thermal image of a fire situated behind a glass window and a direct thermal image of the same fire captured in the 7.5 µm to 13.5 µm wavelength range.

The most common non-contact thermal cameras use microbolometric sensors – a grid of minimalistic thermistors (pixels), all capturing the IR irradiation energy in certain wavelength ranges. This work uses the Wiris Pro thermal camera containing a microbolometric sensor
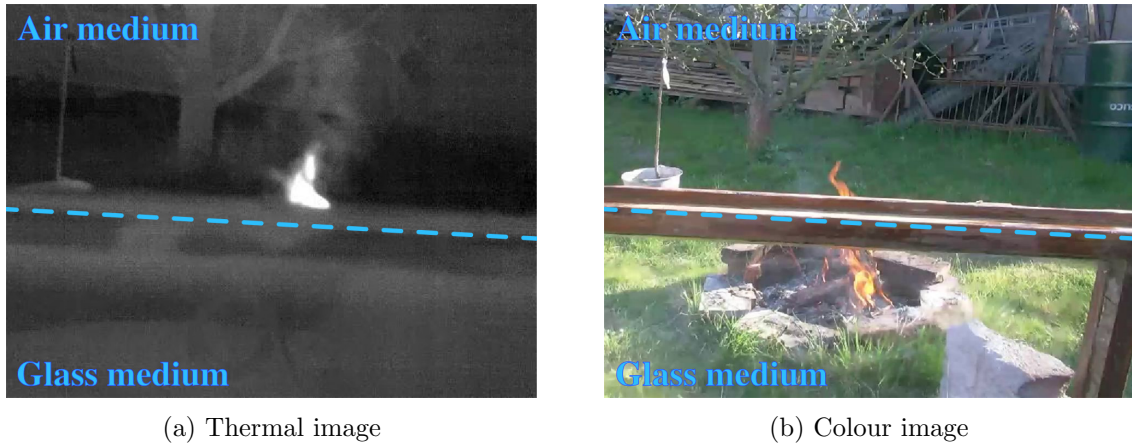
(a) Thermal image   (b) Colour image

Figure 4.1: Influence of a glass medium on thermal imaging — the IR radiation is completely absorbed by common glass medium.

with a wavelength range of $7.5\,\mu\text{m}$ to $13.5\,\mu\text{m}$. As stated before, glass absorbs radiation in this wavelength range and is therefore opaque for the used thermal camera (see Figure 4.1). This limits the usage of the designed fire detection system only to clear UAV-fire visibility applications.

4.1.2 Fire detection in thermal images

The purpose of the fire detection subsystem is to provide information about the fire presence in the thermal image, to estimate the fire position in the image, and to perform a simple analysis of the object. The analysis shall contain information about the maximal temperature of a burning object, an area of the fire in the image, and a parameter estimating the power of the fire.

Due to the high contrast in temperature of burning objects and the ambient temperature, the proposed fire detection system follows a threshold-based methodology. The method follows pseudocode given in Algorithm 1. The algorithm starts with a pixel wide temperature thresholding, which decides whether the temperature measured by a pixel is larger than a marginal temperature threshold T_t [°C]. The marginal temperature was calibrated to $T_t = 300\,°\text{C}$ since this temperature is not common in a general environment and it allows for the detection of small-scale fires (see Figure 4.2 for the thermal image of a small cooker).

Neighbouring pixels with temperature larger than the threshold T_t are joined to a set $\mathcal{T}_i$. Each set $\mathcal{T}_i$ is bordered by its bounding box, which is a minimal rectangle containing the full set of pixels (see Figure 4.3). Given a thermal image $\mathcal{I}$, the Algorithm 1 iteratively initiates a flood-fill procedure (see [70]) starting from the pixel with the maximal temperature exceeding T_t. At the end of each iteration i, the grouped set of pixels $\mathcal{T}_i$ outputted by the flood-filling is then removed from the image $\mathcal{I}$ as

$$\mathcal{I} = \mathcal{I} \setminus \mathcal{T}_i. \tag{4.5}$$

The algorithm finishes when there is no pixel with measured temperature above threshold T_t. The pixel with the maximal temperature within the $\mathcal{T}_i$ is saved and used afterward for fire
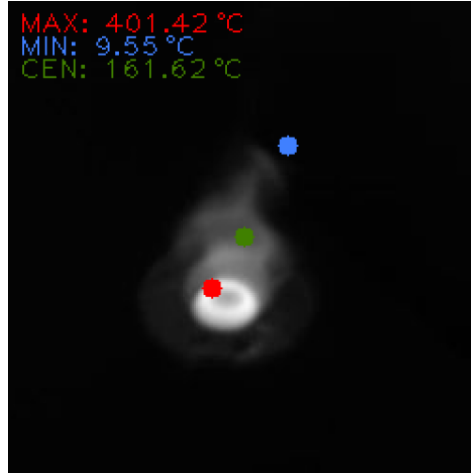
Figure 4.2: Contrast between a fire and the ambient temperature.

localization in 3D (see Section 4.2). As shown in Figure 4.3a, the flood-fill procedure outputs many mutually separated objects. To process the output of the flood-filling procedure, the overlapping bounding boxes of sets $\mathcal{T}_i$ are merged together. This makes the detection output cleaner and more robust (see Figure 4.3b). Algorithm 1 is followed by a simple analysis of the properties of the detected fire hypotheses. These properties are the area of an object in the thermal image and the radiant flux produced by the fire in the direction of the thermal camera.

(a) Fires detection before bounding boxes merging.

(b) Fires detection after bounding boxes merging.

Figure 4.3: Detection of multiple fires in a single thermal image using Algorithm 1. Detection artifacts (a) are removed by merging the overlapping bounding boxes (b).

The number of pixels in $\mathcal{T}_i$ is used to estimate the dimensions of the fire. To estimate the dimensions in real-world units, the average distances d_i [m] of the projected objects to each pixel in $\mathcal{T}_i$ are assumed to be known – see Section 4.2 for the methodology of measuring the distances d_i. The area represented by a single pixel is an approximation determined as an area of a square with side length a [m]. The square side length can be computed from the

---

Algorithm 1 Fire detection

1: **Input:**
2:     T_t ▷ temperature threshold T_t
3:     $\mathcal{I}$ ▷ thermal image
4: **Output:**
5:     $fires$ ▷ list of detected fires
6: $fires \leftarrow \{\}$ ▷ a new empty list of fires
7: $T_{max} \leftarrow \text{maximum}(\mathcal{I})$ ▷ find maximal temperature
8: $\vec{p}_{max} \leftarrow \text{argmax}(\mathcal{I})$ ▷ find pixel with maximal temperature
9: $i \leftarrow 0$
10: **while** $T_{max} > T_t$ **do**
11:     $\mathcal{T}_i \leftarrow \text{flood\_fill}(\mathcal{I}, \vec{p}_{max}, T_t)$ ▷ get the pixel set $\mathcal{T}_i$ by flood filling
12:     $\mathcal{I}(\mathcal{T}_i) \leftarrow -\infty$ ▷ remove $\mathcal{T}_i$ from the image
13:     $T_{max,i} \leftarrow T_{max}$ ▷ save maximum measured temperature
14:     $\vec{p}_{max,i} \leftarrow \vec{p}_{max}$ ▷ save fire maximum temperature position
15:     $fire \leftarrow \{\mathcal{T}_i, T_{max,i}, \vec{p}_{max,i}\}$
16:     $fires.\text{add}(fire)$ ▷ add new fire to the list of hypotheses
17:     $T_{max} \leftarrow \text{maximum}(\mathcal{I})$ ▷ find maximal temperature
18:     $\vec{p}_{max} \leftarrow \text{argmax}(\mathcal{I})$ ▷ find pixel with maximal temperature
19:     $i \leftarrow i + 1$
20: **end while**
21: $fires = \text{merge\_overlapping\_bounding\_boxes}(fires)$ ▷ connect hot places to one fire

---

camera resolution and the camera field of view (FoV) as

$$a_i = d_i \frac{\alpha}{S}, \tag{4.6}$$

where α [rad] is the horizontal or the vertical FoV in radians and S [-] corresponds to the image width or the image height in pixels. The area A_i [m^2] of a fire hypothesis $\mathcal{T}_i$ in real-world units is then approximated as

$$A_i = N_i \, a_i^2 = \frac{N_i \, d_i^2 \, \alpha^2}{S^2}, \tag{4.7}$$

where

$$N_i = \left| \mathcal{T}_i \right| \tag{4.8}$$

is the total number of pixels of detection hypothesis $\mathcal{T}_i$ and d_i is average distance of all pixels in $\mathcal{T}_i$.

The strength of a fire hypothesis $\mathcal{T}_i$ can be characterized by the radiant flux Φ_{ei} [W] produced by the fire area A_i seen by the camera. The radiant flux can be computed as

$$\Phi_{ei} = M_{ei} \, A_i \tag{4.9}$$

where A_i is the estimated seen area of the fire and M_{ei} [W m^{-2}] is the radiant exitance emitted by the fire in area A_i. The radiant exitance is given by the Stefan–Boltzmann law. Because the emissivity of the burning object is unknown, the object is assumed to be the black body. This yields an estimation of maximal possible radiant flux produced by the fire. Due to the

estimation of the maximal possible power, the maximum measured fire temperature is used in the Stefan–Boltzmann law. The estimated maximum radiant flux produced by the fire is

$$\Phi_{ei} = A_i\, M_{ei} = A_i\, \sigma\, \varepsilon\, T_{max,\,i}^4 = A_i\, \sigma\, T_{max,\,i}^4, \tag{4.10}$$

where $T_{max,\,i}$ [°C] is the maximal temperature of the analysed fire.

4.2 Fire localization

The task of a fire localization system is to estimate the relative 3D position of detected fires in the image taken by the onboard thermal camera. This system fuses data provided by the fire detection system (see Section 4.1) with data provided by other onboard sensors. These sensors provide information about the distance between the UAV and its environment. The fusion of fire hypotheses and distance measurements takes also into account the filtering of false positives and tracking of the hypotheses in time. This improves the performance and accuracy of the estimation.

4.2.1 Depth camera

An onboard 3D camera provides a stream of depth images — the value of each pixel encodes the distance to the projected scene. The proposed design uses Intel Realsense D435i depth camera, mounted onboard the UAV such that the optical axis of the depth camera axis is parallel to the optical axis of the thermal camera. The principle of this particular sensor is the depth estimation from a stereo-pair (see [71]) of IR cameras detecting features of an IR pattern projected to the scene. As the used sensor projects pattern in the same spectrum (IR) heavily polluted by radiation from the desired measured objects (fires), the performance of the sensor is analyzed in real-world scenarios.

The depth estimation performance of Intel Realsense D435i was tested on data with clear visibility to an open fire. The data showed no influence on the depth estimation for small-scale fires (see Figure 4.4). For highly bright fires (see Figure 4.5), the IR emission influences the accuracy of the estimation in the emission source and its close neighborhood by creating artifacts (holes) in the data. However, there remains enough depth data sufficient for averaging in a local neighborhood.
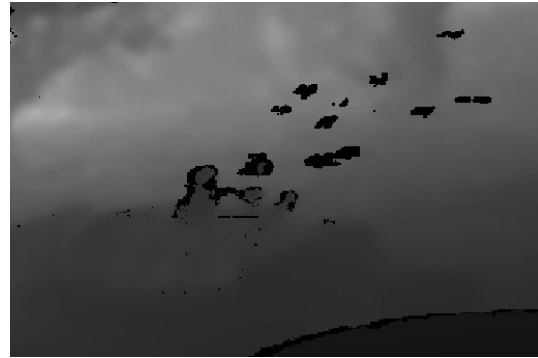
(a) RGB image   (b) Depth data from Intel Realsense D435i

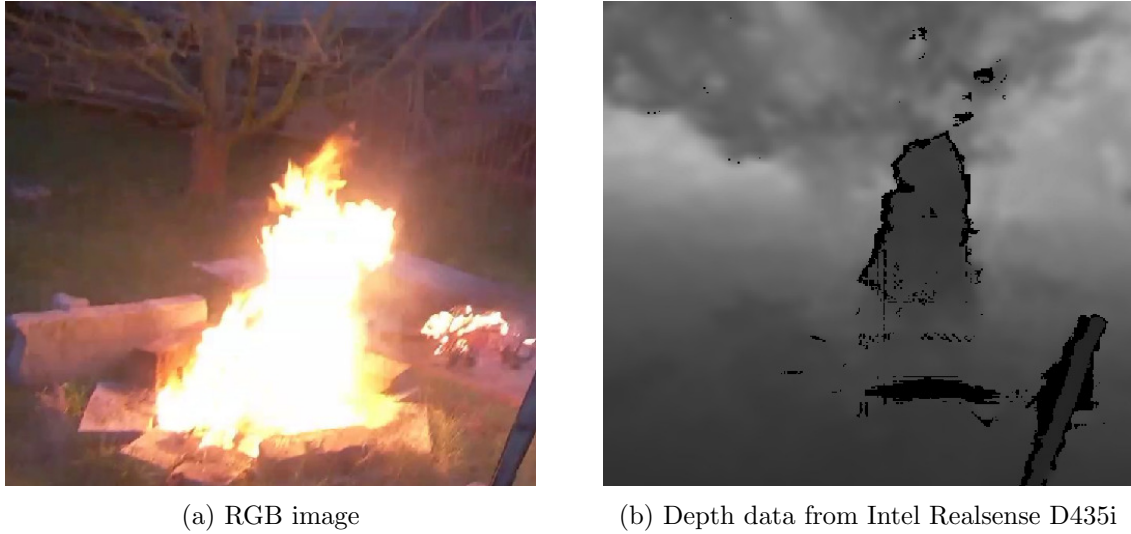Figure 4.4: Depth estimation in a scene with a burning fire.

(a) RGB image

(b) Depth data from Intel Realsense D435i

Figure 4.5: Disturbance in depth estimation in scene with a bright fire.

4.2.2 Projection of fire detections to world

To project fire detections from the 2D image into 3D space, the designed method uses a 3D depth camera. The final projection depends on parameters of the thermal and the depth camera, on the models of the cameras, and the transformation between the two camera coordination frames. To model the cameras, there exist several mathematical concepts [72] — the most common, and here also employed, concept is the pinhole camera model. The pinhole camera model projects the 3D point onto the image plane of an ideal pinhole camera with point aperture. Although real-world cameras incorporate inaccuracies, this model is commonly used for common cameras with narrow lenses. This elementary mathematical model can be simply characterized by a camera matrix (projection matrix) which maps 3D points to 2D image plane of the camera.

The projection matrix $\mathbf{C} \in \mathbb{R}^{3 \times 4}$ specifies the projection of a real point in 3D space to a 2D image plane. The matrix $\mathbf{C}$ hence represents the relations between the homogeneous coordinates $\vec{x} \in \mathbb{R}^{4 \times 1}$ [m] of a real 3D point in camera coordination system and the homogeneous coordinates of its 2D projection

$$\vec{y} = \mathbf{C}\vec{x}, \, y \in \mathbb{R}^{3 \times 1} \tag{4.11}$$

in the image plane. With respect to coordination systems defined in Figure 4.6, the camera matrix is defined as

$$\mathbf{C} = \begin{bmatrix} f_l & 0 & 0 & c_x \\ 0 & f_l & 0 & c_y \\ 0 & 0 & 1 & 0 \end{bmatrix}, \tag{4.12}$$

where c_x and c_y are pixel coordinates of the pinhole in the image coordination frame and f_l is the focal length of the camera in pixels. In real world, the camera matrix is determined by a geometric camera calibration [73], which can estimate its parameters.
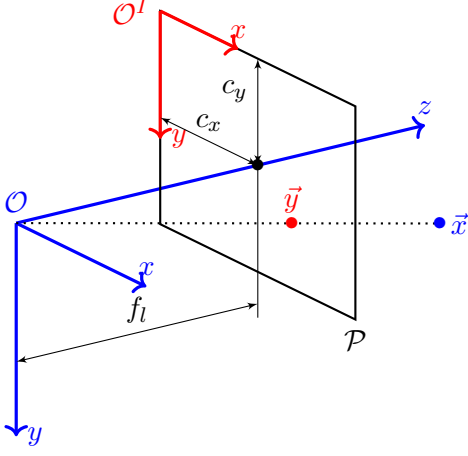
Figure 4.6: Coordination system of a camera $\mathcal{O}$ and its image plane $\mathcal{P}$ with coordination system $\mathcal{O}^I$.
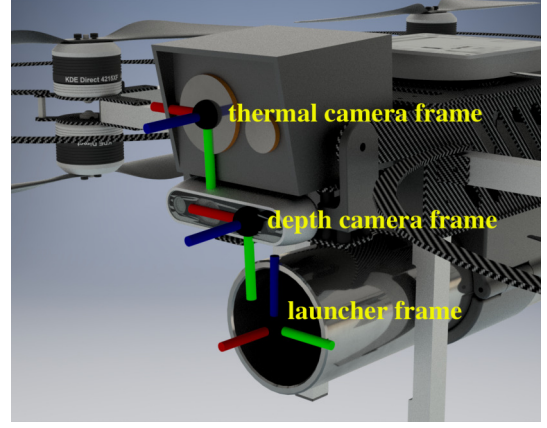

Figure 4.7: UAV coordination frames. X-axis is red, Y-axis is green, and Z-axis is blue.

This camera model can be used for both the thermal camera and the depth camera. With known transformation among the coordination frames of the cameras, the pixel coordinates in the thermal image plane can be projected into the image plane of the depth camera. Let the coordination frames of both the cameras follow the conception illustrated in Figure 4.6, and let the thermal camera be specified by its camera matrix $\mathbf{C}_t \in \mathbb{R}^{3 \times 4}$ and the depth camera by its camera matrix $\mathbf{C}_d \in \mathbb{R}^{3 \times 4}$. Let also $\vec{x}_t \in \mathbb{R}^{4 \times 1}$ [m] be the homogeneous coordinates of a 3D point X in the thermal camera frame and $\vec{x}_d \in \mathbb{R}^{4 \times 1}$ [m] be the homogeneous coordinates of the same point in the frame of the depth camera. Further, the transformation matrix $\mathbf{T}_t^d \in \mathbb{R}^{4 \times 4}$ represents the transformation from the thermal camera frame to the depth camera frame (see Figure 4.7 for its placement on the UAV), such as

$$\vec{x}_d = \mathbf{T}_t^d \, \vec{x}_t. \tag{4.13}$$

The defined camera matrices can be used to project a point $\vec{x}_t$ to the thermal image plane as

$$\vec{x}_t^I = \mathbf{C}_t \, \vec{x}_t, \; \vec{x}_t^I \in \mathbb{R}^{3 \times 1}. \tag{4.14}$$

Similarly, the same holds for a point $\vec{x}_d$ and the depth camera as

$$\vec{x}_d^I = \mathbf{C}_d \, \vec{x}_d, \; \vec{x}_d^I \in \mathbb{R}^{3 \times 1}. \tag{4.15}$$

These relations are also visualized in Figure 4.8.

To project a given $\vec{x}_t^I$ (fire detection in the thermal image plane – see Section 4.1.2) to a 3D point X, a set of solutions $\mathcal{Y}$ to Equation 4.14 needs to be found for unknown $\vec{x}_t \in \mathcal{Y}$. The set $\mathcal{Y}$ consists of all points on line $\mathcal{Y}$ intersecting the thermal camera origin and pixel $\vec{x}_t^I$, see Figure 4.8 for its illustration. In other words, the set $\mathcal{Y}$ represents all points that can be seen by pixel $\vec{x}_t^I$ of a pinhole camera. However real cameras see only points in front of it, which allows the line $\mathcal{Y}$ to be reduced to a ray $\mathcal{R}$

$$\mathcal{R} = \{\vec{x}_t = \vec{u} \, r \,|\, [0 \; 0 \; 1 \; 0] \, \vec{x}_t > 0, \, \vec{u} \in \mathbb{R}^{4 \times 1}, \, r \in \mathbb{R}\}, \tag{4.16}$$

where $\vec{u} \in \mathbb{R}^{4 \times 1}$ is a normalized particular solution to Equation 4.14

$$\vec{u} \in \{\vec{u} \mid \mathbf{C}_t \, \vec{u} = \vec{x}_t^I, \, \|\vec{u}\| = 1, \, \vec{u} \in \mathbb{R}^{4 \times 1}\}. \tag{4.17}$$
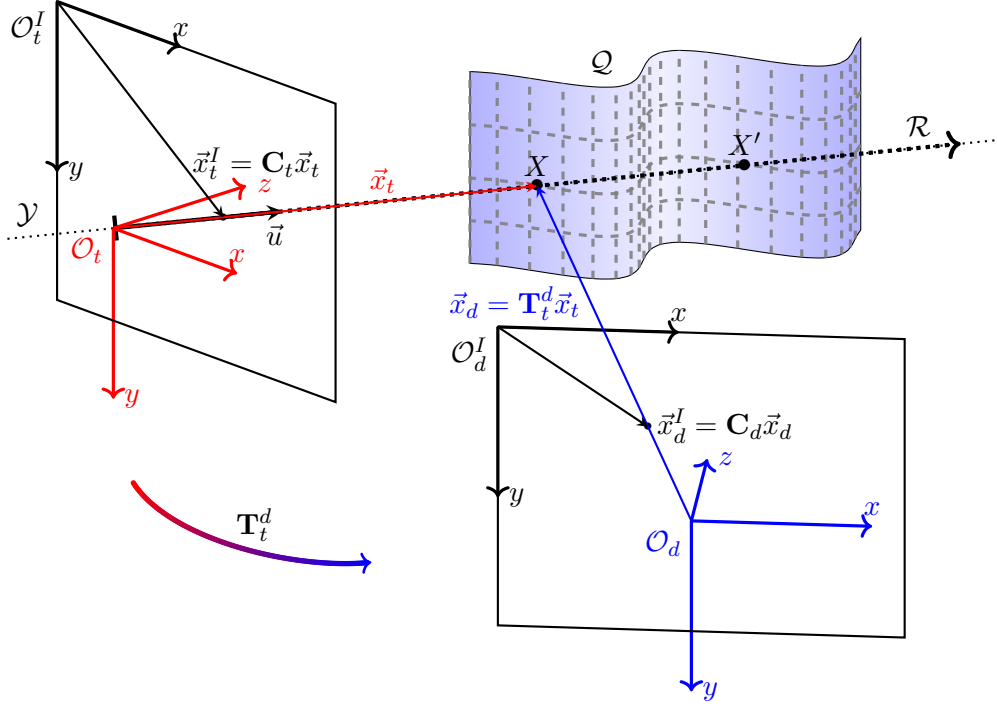

Figure 4.8: Projection of point in thermal image plane $\vec{x}_t^I$ to 3D point X. $\mathcal{O}_t$ is the thermal camera frame, $\mathcal{O}_d$ is the depth camera frame, $\mathcal{O}_t^I$ is the thermal image coordination system, $\mathcal{O}_d^I$ is the depth image coordination system, and $\mathcal{Q}$ is the surface seen by cameras.

Let $\mathcal{X} = \mathcal{R} \cap \mathcal{Q}$ be a set of intersections of ray $\mathcal{R}$ and surface $\mathcal{Q}$ seen by both the cameras. The surface $\mathcal{Q}$ is defined by the depth camera data in form of function $d(\vec{v})$ [m] returning the Euclidean distance between the depth camera XY-plane and the surface $\mathcal{Q}$ seen by pixel $\vec{v}$. Hence a point X lays on surface $\mathcal{Q}$ if

$$[0 \; 0 \; 1 \; 0] \, \vec{x}_d = d(\mathbf{C}_d \, \vec{x}_d). \tag{4.18}$$

Equation 4.18 can be rewritten using Equation 4.13 and Equation 4.16 as

$$[0 \; 0 \; 1 \; 0] \, \mathbf{T}_t^d \, \vec{u} \, r = d(\mathbf{C}_d \, \mathbf{T}_t^d \, \vec{u} r). \tag{4.19}$$

As visualized in Figure 4.8 there can be multiple solutions to Equation 4.19, but the thermal camera sees in principle only one — the nearest. Therefore the length r of vector $\vec{x}_t$ is found using minimization task

$$
\begin{aligned}
r^* = {}& \min r \\
\text{subject to} \quad & r \in \mathbb{R} \\
& [0 \; 0 \; 1 \; 0] \, \mathbf{T}_t^d \, \vec{u} \, r = d(\mathbf{C}_d \, \mathbf{T}_t^d \, \vec{u} r) \\
& [0 \; 0 \; 1 \; 0] \, \vec{u} \, r \geq 0 \\
& \vec{x}_t^I = \mathbf{C}_t \, \vec{u} \, r.
\end{aligned}
\tag{4.20}
$$

Using $r*$ allows to simplify Equation 4.16 and hence to project the 2D detection into the world as

$$\vec{x}_t = \vec{u}\, r^* \tag{4.21}$$

in the thermal camera frame or

$$\vec{x}_d = \mathbf{T}_t^d\, \vec{u}\, r^* \tag{4.22}$$

in the depth camera frame.

Implementation of the entire projection pipeline is described in more detail in Section 4.2.3.

4.2.3 Fire localization algorithm

To find a solution to Equation 4.20, the designed algorithm (see Algorithm 2) finds an approximation respecting limitations of real world. The algorithm takes advantage of knowledge about the maximum measurement range of Intel Realsense D435i $r_m = 10\,\text{m}$ [65] and about the functionality of the fire extinguishing ampoule. The ampoule is capable to influence fire sources in a spread area and hence the desired accuracy of fire localization can be reduced to tens of centimeters.

The designed method follows the algorithm rewritten in pseudocode in Algorithm 2. The algorithm takes normalized particular solution $\vec{u}$ given by Equation 4.17 and orients it to the direction of the camera optical axis. The vector $\vec{u}$ is provided by function `CameraModel.getRay(`C_t`, `$\vec{x}_t^I$`)`, which does inverse process to the camera projection. This vector is then scaled to maximum measurement range of the sensor and is discretized to a resolution of $r_d = 5\,\text{cm}$. The discretization yields a set of testing points

$$\vec{x}_{t,j} \in \mathcal{S} = \left\{ r_d\, j\, \vec{u} \,\Big|\, j \in \left\{ 0, 1, \cdots, \frac{r_m}{r_d} \right\} \right\}. \tag{4.23}$$

These points are then transformed to the coordination frame of the depth camera and projected to the image plane of the depth camera as

$$\vec{x}_{d,j}^I = \mathbf{C}_d\, \vec{x}_{d,j} = \mathbf{C}_d\, T_t^d\, \vec{x}_{t,j}. \tag{4.24}$$

The feasibility of the projected points $\vec{x}_{d,j}$ is verified with respect to a distance of seen surface $d(\vec{x}_{d,j}^I)$ [m] measured by the depth camera on pixel with coordinates $\vec{x}_{d,j}^I$. Let $z_{d,j}$ [m] be the Z-coordinate of vector $\vec{x}_{d,j}$ such as

$$z_{d,j} = [0\ 0\ 1\ 0]\, \vec{x}_{d,j}. \tag{4.25}$$

Then the points set of ray-surface intersections $\mathcal{X}$ is given as

$$\mathcal{X} = \mathcal{R} \cap \mathcal{Q} = \left\{ \frac{x_{d,j} + x_{d,j+1}}{2} \,\bigg|\, z_{d,j} <= d(\vec{x}_{d,j}^I) < z_{d,j+1}, j \in \left\{ 0, 1, \cdots, \frac{r_m}{r_d} \right\} \right\}. \tag{4.26}$$

However the above equation has solution only in ideal case, where all $d(\vec{x}_{d,j}^I)$ are defined. In real world, data in certain pixels of the depth image might be unavailable.

Algorithm 2 Fire localization

1: **Input:**
2:     $\vec{x}_t^I$ ▷ fire detection hypothesis pixel coordinates
3:     $\mathbf{T}_t^d$ ▷ transformation matrix between camera frames
4:     $\mathbf{C}_d$ ▷ depth camera projection matrix
5:     $\mathbf{C}_t$ ▷ thermal camera projection matrix
6:     r_d ▷ discretization resolution
7:     r_m ▷ maximum localization range
8: **Output:**
9:     $\vec{x}_d$ ▷ 3D hypothesis position in the depth camera frame
10: $\vec{u} \leftarrow \text{CameraModel.getRay}(\mathbf{C}_t, \vec{x}_t^I)$ ▷ particular solution $\vec{u}$ to Equation 4.14
11: **if** $[0\ 0\ 1\ 0]\,\vec{u} < 0$ **then**
12:     $\vec{u} \leftarrow -\vec{u}$ ▷ match orientation of $\vec{u}$ with the camera optical axis
13: **end if**
14: $\vec{u} \leftarrow \frac{\vec{u}}{\|\vec{u}\|}$ ▷ normalize the particular solution
15: $bigger\_last \leftarrow$ **false**   ▷ initialize value for first loop
16: **for** $j \in \left\{0, 1, \cdots, \frac{r_m}{r_d}\right\}$ **do**
17:     $\vec{x}_{t,j} \leftarrow r_d\,j\,\vec{u}$ ▷ discretize to max measurement range with 5cm step
18:     $\vec{x}_{d,j} \leftarrow \mathbf{T}_t^d\,\vec{x}_{t,j}$ ▷ transform to the depth camera frame
19:     $\vec{x}_{d,j}^I \leftarrow \mathbf{C}_d\,\vec{x}_{d,j}$ ▷ project the point to the depth camera image plane
20:     **if** $\text{valid}(x_{d,j}^I) >= 0.6$ **then**   ▷ if valid depth data in $\vec{x}_{d,j}^I$ exist
21:         $m_j \leftarrow \text{measure}(x_{d,j}^I)$ ▷ measure depth in $\vec{x}_{d,j}^I$
22:         $bigger \leftarrow m_j > [0\ 0\ 1]\,\vec{x}_{d,j}$ ▷ $\vec{x}_{d,j}$ is in front of seen surface
23:         **if** $\neg bigger \wedge bigger\_last$ **then** ▷ $\mathcal{R}$ intersect surface between current and last $\vec{x}_{d,j}$
24:             $\vec{x}_d \leftarrow \frac{\vec{x}_{d,j}+\vec{x}_{d,j-1}}{2}$ ▷ return middle point between current and last $\vec{x}_{d,j}$
25:             **return** $\vec{x}_d$
26:         **end if**
27:         $bigger\_last \leftarrow bigger$ ▷ store values for next loop
28:     **end if**
29: **end for**

As the depth data contain holes (non-defined pixels), the distance m_j [m] is assumed to be the average distance in squared local neighborhood of the pixel $\vec{x}^I_{d,j}$, such as

$$m_j = \text{measure}(x^I_{d,j}) = \frac{1}{n_j} \sum_{k=-h}^{h} \sum_{l=-h}^{h} d\left(\vec{x}^I_{d,j} + [k \; l \; 1]^T\right), \tag{4.27}$$

where h is pixel size of the neighborhood and n_j is the number of pixels containing valid data within the neighborhood. If no more than 60% of pixels in the local neighborhood contain valid data

$$\text{valid}(x^I_{d,j}) = \frac{n_j}{h^2} < 0.6, \tag{4.28}$$

the pixel is evaluated as undefined and the set $\mathcal{X}$ defined in Equation 4.26 is given as

$$\mathcal{X} = \emptyset. \tag{4.29}$$

Let $\mathcal{M}$ be the set set of all valid valid measurements

$$\mathcal{M} = \left\{ m_j \; \middle| \; \text{valid}(j) >= 0.6, j \in \left\{0, 1, \cdots, \frac{r_m}{r_d}\right\} \right\}, \tag{4.30}$$

$\mathcal{V}$ valid measurements set of all $\vec{x}_{d,j}$ with Z-coordinate z_j greater than m_j

$$\mathcal{V} = \left\{ \vec{x}_{d,j} \; \middle| \; z_j > m_j, m_j \in \mathcal{M}, j \in \left\{0, 1, \cdots, \frac{r_m}{r_d}\right\} \right\}, \tag{4.31}$$

and $\mathcal{W}$ be the set set of all $\vec{x}_{d,j}$ with Z-coordinate z_j lower than m_j

$$\mathcal{W} = \left\{ \vec{x}_{d,j} \; \middle| \; z_j < m_j, m_j \in \mathcal{M}, j \in \left\{0, 1, \cdots, \frac{r_m}{r_d}\right\} \right\}. \tag{4.32}$$

Then the Equation 4.26 can be approximated as

$$\mathcal{X} = \left\{ \frac{\vec{x}_{d,a} + \vec{x}_{d,b}}{2} \; \middle| \; a < b, \, a \in \mathbb{N}, \, b \in \mathbb{N}, \, \vec{x}_{d,a} \in \mathcal{W}, \, \vec{x}_{d,b} \in \mathcal{V}, \, \forall_{k \in \{a, \cdots, b\}} \, m_k \notin \mathcal{M} \right\}. \tag{4.33}$$

The final $\vec{x}_d$ which is coordination of point X in depth camera frame is found as

$$\vec{x}_d = \min_{\vec{x}_{d,c} \in \mathcal{X}} (\|\vec{x}_{d,c}\|). \tag{4.34}$$

To cope with noise and IR reflections from neighboring materials, both producing false detections, the algorithm tracks the spatial hypotheses in time. If a hypothesis is detected for t_d [s], it is marked as confirmed and is further published as an available target for fire extinguishing. Tracking of the hypotheses in time is done by comparing the spatial detections in two consecutive thermal images $\mathcal{I}$ and $\mathcal{J}$. The comparison is done by comparing the characteristic attributes (position, area, and maximal temperature) of the hypotheses in two consequent frames. Let image $\mathcal{I}$ be an observation taken one time step prior observing image $\mathcal{J}$, then two hypotheses $\mathcal{T}_i \subset \mathcal{I}$ and $\mathcal{T}_j \subset \mathcal{J}$ are marked as identical if

$$\mathcal{T}_j = \arg\max_{\mathcal{T}_k \subset \mathcal{J}} \left(A\left(\mathcal{T}_k, \mathcal{T}_i\right) \right) \tag{4.35}$$

and

$$\left| \max_{T \in \mathcal{T}_i}(T) - \max_{T \in \mathcal{T}_j}(T) \right| < T_d \max_{T \in \mathcal{T}_i}(T), \tag{4.36}$$

where T_d is maximal temperature difference in percent calibrated to $T_d = 30\%$, $T \in \mathcal{T}_l$ represents temperature of any pixel in hypothesis $\mathcal{T}_l$, and $A(\mathcal{T}_k, \mathcal{T}_i)$ is common pixel area of bounding boxes of hypotheses $\mathcal{T}_k$ and $\mathcal{T}_i$. The longevity of a hypothesis is prolonged if the hypothesis is seen in two consequent frames. If a hypothesis was not detected again for t_n [s], the hypothesis is classified as false detection and is discarded.

4.3 Fire locking

Given a confirmed hypothesis (detected and localized fire), the UAV needs to be positioned optimally with respect to the ballistic curve of the ampoule launcher. The ballistic curve [74] represents a mathematical description of a falling object with non-zero horizontal velocity (see Figure 4.9). In this section, the ballistic curve is described in detail. In Section 5.3.5, the parameters of the launcher mechanism used in our design are empirically derived from real-world experiments.

Each falling object with non zero initial horizontal velocity follows the ballistic curve. The mathematical description of the curve can be derived from a differential equation for motion of a mass point $\vec{p}(t)$ [m] with a non-zero initial velocity within a gravitational field. Shape of the ballistic curve depends on the mass of the falling object m [kg], the initial velocity $\vec{v}_0$ [m s^{-1}], and dissipation of the kinetic energy in the environment. If there is no dissipation, the trajectory has a parabolic shape. For low velocities of a mass point, the dissipation is assumed to be proportional to the actual velocity of the mass point $\frac{d\vec{p}(t)}{dt}$ [m s^{-1}]. For higher velocities, the dissipation force is described by more complex formula also lift force become indispensable (see [75] for details). The model for higher velocities is highly complex [76] and can not provide elementary relation between coordinations of the mass point. Our design assumes low velocity of the launched projectile and hence the dissipation force is assumed to be proportional to the projectile velocity. In such case, the dissipation force is given as

$$F_d = -h \frac{d\vec{p}(t)}{dt} \text{ [N]}, \tag{4.37}$$

where h [kg s^{-1}] is a coefficient of friction depending on the shape of the falling object and viscosity of the ambient environment. Mathematical formula of the ballistic curve, where the gravitational acceleration is oriented in the reversed direction of the Z-axis and the mass point is located in the origin of the projectile, is described by the differential equation of motion

$$\frac{d^2\vec{p}(t)}{dt^2} = -\frac{h}{m} \frac{d\vec{p}(t)}{dt} - g[0\ 0\ 1]^T, \tag{4.38}$$

where g [m s^{-2}] is the gravitational acceleration of Earth and t [s] is time. Given at time $t = 0$ s an initial velocity $\vec{v}_0$ and an initial position $\vec{p}_0$, the solution to Equation 4.38 is given as

$$\vec{p}(t) = \frac{m}{h} \left(\vec{v}_0 + \left[0\ 0\ \frac{mg}{h} \right]^T \right) \left(1 - e^{-\frac{ht}{m}} \right) - \left[0\ 0\ \frac{mg}{h}t \right]^T + \vec{p}_0. \tag{4.39}$$

Equation 4.39 can be expressed with respect to the launcher coordination frame of the designed system in Figure 4.7. Given a desired horizontal distance l_h [m] from the launcher, the solution can be expressed as

$$\vec{p}(l_h) = \begin{bmatrix} l_h \\ 0 \\ \frac{gm}{v_0\,h}l_h + \frac{m^2 g}{h^2}\ln\left(1 - \frac{hl_h}{m\,v_0}\right) \end{bmatrix}, \tag{4.40}$$

where v_0 is the muzzle velocity of the ampoule in the X-axis direction of the launcher. Together with a known UAV position (and hence the launcher position), Equation 4.40 can be used for estimation of the optimal position for launching the fire extuinguisingh ampoule into the detected fire.

The simplest way to position the UAV in order to discharge the ampoule to the fire is to rotate the UAV towards the fire and only control the altitutde of the UAV. To rotate the UAV towards the fire, the desired change of heading (azimuth) of the UAV is computed as

$$\phi = \text{atan2}([0\ 1\ 0\ 0]\,\vec{x}_l, [1\ 0\ 0\ 0]\,\vec{x}_l) \tag{4.41}$$

where $\vec{x}_l$ is is the 3D position of the fire hypothesis in the launcher coordination frame. The position is given as

$$\vec{x}_l = \mathbf{T}_d^l\,\vec{x}_d, \tag{4.42}$$

where $\mathbf{T}_d^l$ is a static transform matrix between the depth camera and the launcher coordination frames, and $\vec{x}_d$ is the position of a fire hypothesis (localized by Algorithm 2) in the depth camera frame. The desired change in altitude is deduced from the ballistic curve after the change in heading is applied to the UAV as

$$l_v(l_h) = [0\ 0\ 1\ 0]\,\vec{x}_l - \frac{gm}{v_0 h}l_h - \frac{m^2 g}{h^2}\ln\left(1 - \frac{hl_h}{mv_0}\right), \tag{4.43}$$

where l_h is the horizontal distance to the fire:

$$l_h = \left\| \begin{bmatrix} 1 & 0 & 0 & 0 \\ 0 & 1 & 0 & 0 \end{bmatrix} \vec{x}_l \right\|.$$
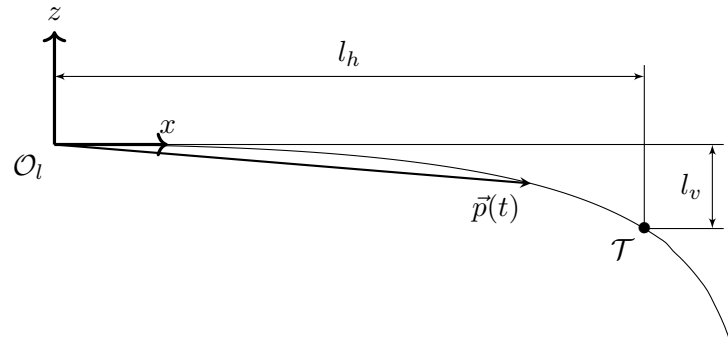

Figure 4.9: Ballistic curve given by Equation 4.40. $\mathcal{O}_l$ is the launcher frame, $\vec{p}(t)$ is the ballistic curve given by Equation 4.39, $\mathcal{T}$ is the target hypothesis (the fire), and l_h and l_v are horizontal and vertical coordinates of $\mathcal{T}$ in $\mathcal{O}_l$.

Chapter 5: Experimental Verification

Contents

The designed system for fire detection and localization is tested in simulation as well as in real-world conditions. In simulation conditions, the system is used for fire localization and UAV positioning in a simulated scenario of a burning tall building. In multiple real-world tests, the system is used to localize static sources of fire on-board the application-tailored UAV platform (see Chapter 3). The methodology used for evaluation of the system performance is further described. The quantitative and qualitative performance of the system (see Chapter 4) is then analyzed and discussed.

5.1 Evaluation metrics

5.1.1 Image classification

The quality of the fire detection system is described by characteristics commonly used for binary classifiers closely described in [77]. The binary classifier labels incoming data as positive or negative. The basic characteristic of binary classifiers is the confusion matrix, which can be used to clearly represent other metrics, namely the prediction error, accuracy, false and true positive rates, precision, recall, sensitivity, and specificity. The confusion matrix contains four numbers — true positives, false positives, true negatives, and false negatives. These numbers are described in the following list.

- The true positives TP is the number of data labeled as positive when the monitored attribute was actually present. In this case, it is the number of fire hypotheses containing pixels correctly classified as a fire.

- The false positives FP is the number of data labeled as positive when the monitored attribute was not actually present. In this case, it is the number of fire hypotheses incorrectly classified as a fire in an object-less image.

- The true negatives TN is the number of data labeled as negatives when the monitored attribute was not actually present. In this case, it is the number of thermal images not containing a fire object, where the fire detection algorithm correctly lacks any hypotheses.

- The false negatives FN is the number of data labeled as negatives when the monitored attribute was actually present. In this case, it is the number of fire objects not covered by any fire hypotheses.

5.1.2 Localization accuracy

The quality of localization each fire hypothesis can be described by the distance between the real position of the fire and the predicted position of the fire by the localization system. The distance error is given as

$$e_i = \left\| \vec{f}_w - \mathbf{T}_d^w \, \vec{x}_{d,i} \right\|, \tag{5.1}$$

where $\vec{x}_{d,i}$ is the position of fire hypothesis $\mathcal{T}_i$ predicted by the localization system (see Equation 4.34), $\vec{f}_w$ [m] is the position of the center of the fire in world coordination frame, and $\mathbf{T}_d^w$ is the transformation matrix between the depth camera frame and the world frame. The transformation matrix hence represents the depth camera pose (position and orientation) within the world. The error is counted for each localized hypothesis and used to estimate the root mean square error (RMSE) used for quantitative evaluation. The RMSE [m] is given as

$$\text{RMSE} = \sqrt{\frac{1}{N} \sum_{i=1}^{N} e_i^2} = \sqrt{\frac{1}{N} \sum_{i=1}^{N} \left\| \vec{f}_w - \mathbf{T}_d^w \, \vec{x}_{d,i} \right\|^2}, \tag{5.2}$$

where N is the total number of localized hypotheses. Smaller $RMSE$ yields more accurate localization.

5.2 Simulation analysis

The entire system was firstly tested during simulated flights in the Gazebo simulator around a simulated fire with a known position. This simulated scenario is shown in Figure 5.1 visualizing the Gazebo scenario with airborne UAV and a static ground fire. Within the presented simulated experiment (see the trajectory followed by a UAV in Figure 5.2), the UAV circulated a static fire. During this airborne movement, the static fire was continuously localized onboard the UAV and predicted the optimal position for the launch positioning using a ballistic curve estimated in Section 5.3.5. In the next three sections, the performance of the three systems – image classification, fire localization, and UAV positioning – is analyzed in detail.
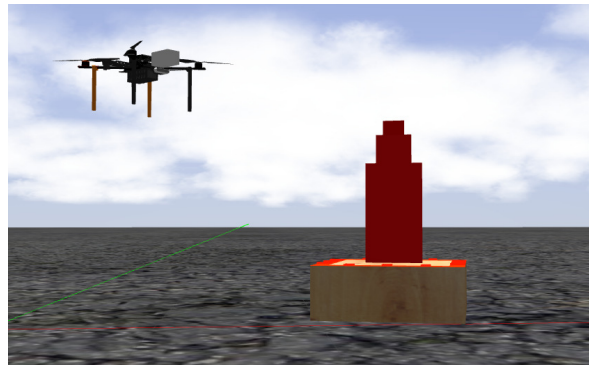
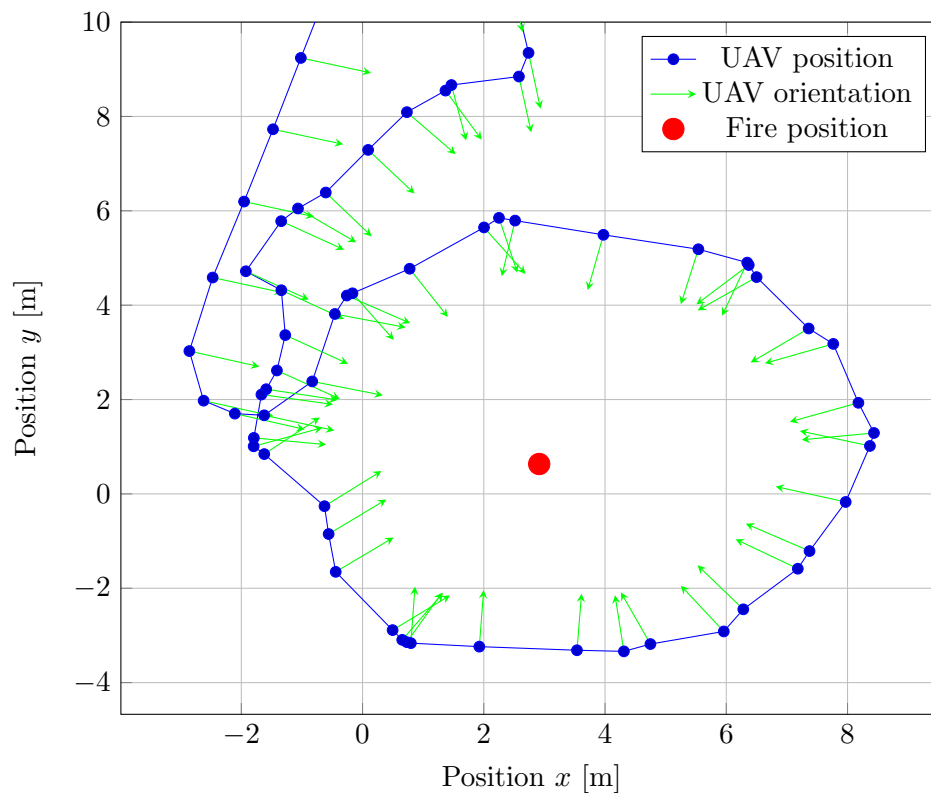Figure 5.1: Visualization of the UAV during the simulated experiment – circulation of the static fire.

Figure 5.2: Trajectory of the UAV during a simulated scenario – circulation of a UAV around a static fire.

5.2.1   Fire classification

The quantitative evaluation of the simulated experiment is summarized in the confusion matrix shown in Table 5.1. The table was obtained with respect to ground truth data – manually labeled images. The same results are also shown in Table 5.2 as other binary classifier characteristics. The results show high detection accuracy in a simulated environment. As the

simulation does not integrate all the real-world constraints, the resulting accuracy points on a high and robust performance of the image classification system.

	Hypothesis	
	positive	negative
Fire present	$TP = 540$	$FN = 3$
Fire not present	$FP = 0$	$TN = 275$

Table 5.1: Confusion matrix as quantitative evaluation of the simulated experiment. As the simulation does not contain all real-world interferences, the ratio of true classifications is high.

Characteristic	Description	Value
prediction accuracy	$ACC = \frac{TP+TN}{TP+TN+FP+FN}$	0.996
prediction error	$ERR = \frac{FP+FN}{TP+TN+FP+FN}$	0.004
false positive rate	$FPR = \frac{FP}{FP+TN}$	0.0
true positive rate = recall	$TPR = \frac{TP}{FN+TP}$	0.994
true negative rate	$TNR = \frac{TN}{FP+TN}$	1.0
precision	$PRE = \frac{TP}{TP+FP}$	1.0

Table 5.2: Qualitative characteristics of the detector measured in simulated experiment.

5.2.2 Fire localization

The fire localization accuracy is described by RMSE error and the absolute error histogram for position error of localized hypotheses. The histogram of absolute localization errors is given in Figure 5.3. The RMSE in the experiment (see Figure 5.2) is 1.011 m. Even though the scenario is simulated, it includes simulation of multiple real-world effects such as the addition of Gaussian and Perlin noise to the depth data, GPS noise, or onboard vibrations. These errors add to the decrease in the localization accuracy.
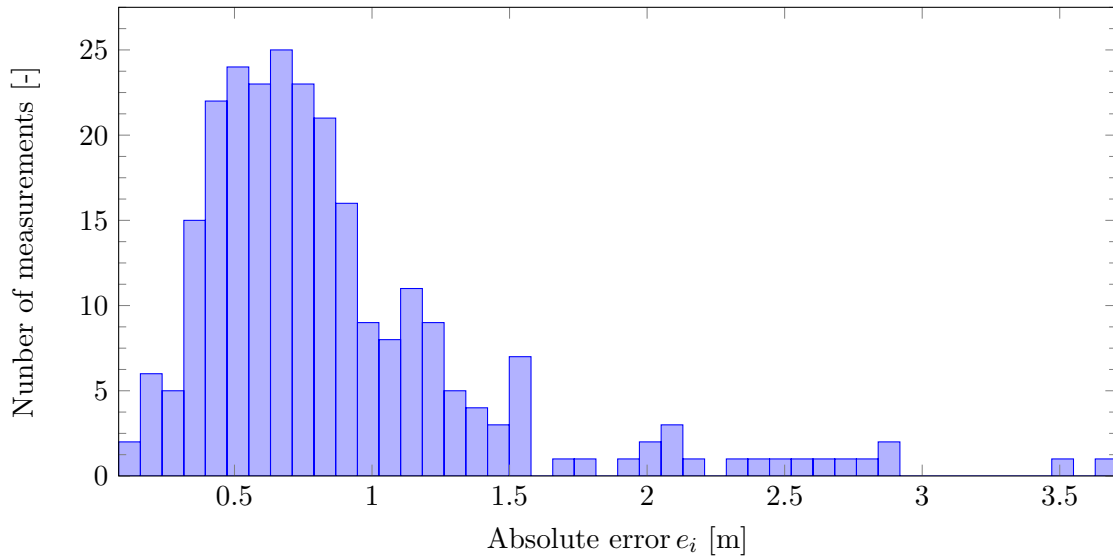
Figure 5.3: Histogram of the absolute error of the fire localization system. During a simulated scenario, the system shows the ability to localize a fire in the world with RMSE 1.011 m.

5.2.3 Fire locking

The fire locking system estimates the optimal position with respect to a detected fire and the ballistic curve of the launched fire extinguishing charge. The proposed strategy (see Section 4.3) for UAV positioning uses the current lateral position and estimates only the heading and altitude of the UAV (and hence the launcher). Using a ballistic curve with parameters estimated later in Section 5.3.5, the performance of the system to estimate the optimal position is evaluated in this section. Figure 5.4 shows the desired (with respect to the current lateral position of the UAV) and the estimated altitude and heading. Even though the estimated optional position depends on fire and UAV localization, bringing inaccuracy to the estimation process, the data shows satisfactory accuracy.
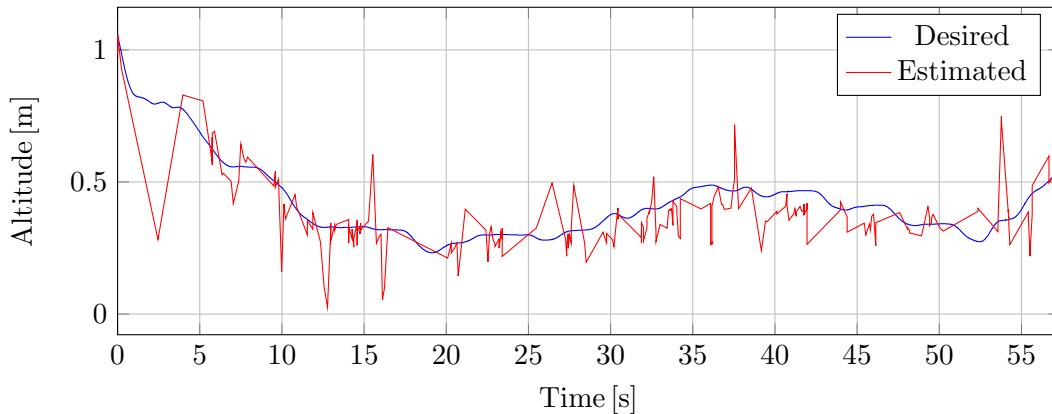
(a) Altitude estimation.
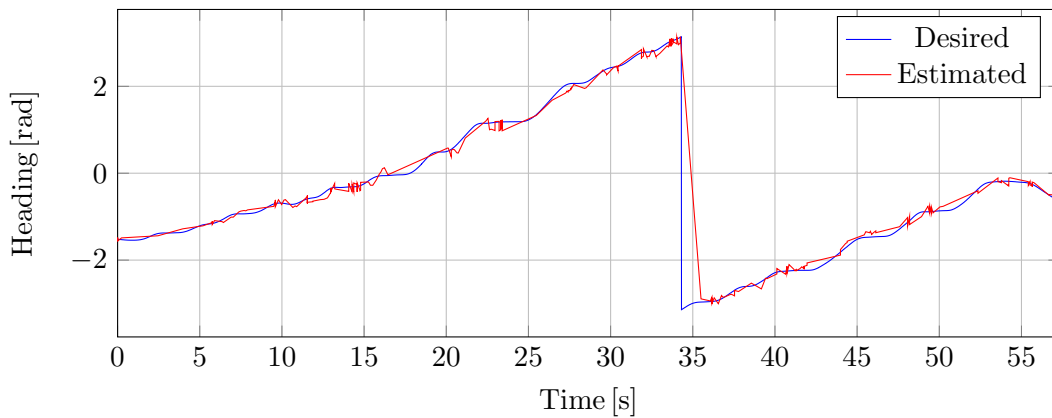
(b) Heading estimation.

Figure 5.4: Position estimation in the simulated experiment (see Figure 5.2). The UAV positioning system estimates the desired altitude and heading, while keeping the lateral position static.

5.3 Real-world experiments

In various real-world experiments, all the designed hardware and software systems were tested. The application-tailored UAV platform (see Chapter 3) was verified to fly in manual mode as well as in autonomous mode using GPS and the MRS system (see Section 2.4). Using the UAV platform, the software systems (image classification, fire localization) were tested onboard the UAV during the further presented real-world experiment. The UAV positioning system was evaluated offline on data recorded during the same experiment. During the experiment, a UAV circulated a static fire (see photo of the experiment in Figure 5.5 and the followed trajectory in Figure 5.6). This experiment is on purpose similar to the simulated scenario. In the next three sections, the performance of the three systems during the real-world experiment is discussed. The experiment can be found within multimedia materials available at `mrs.felk.cvut.cz/theses/nydrle2020`.

Figure 5.5: Photo of the application-tailored UAV during the real-world experiment – circulation of the static fire.
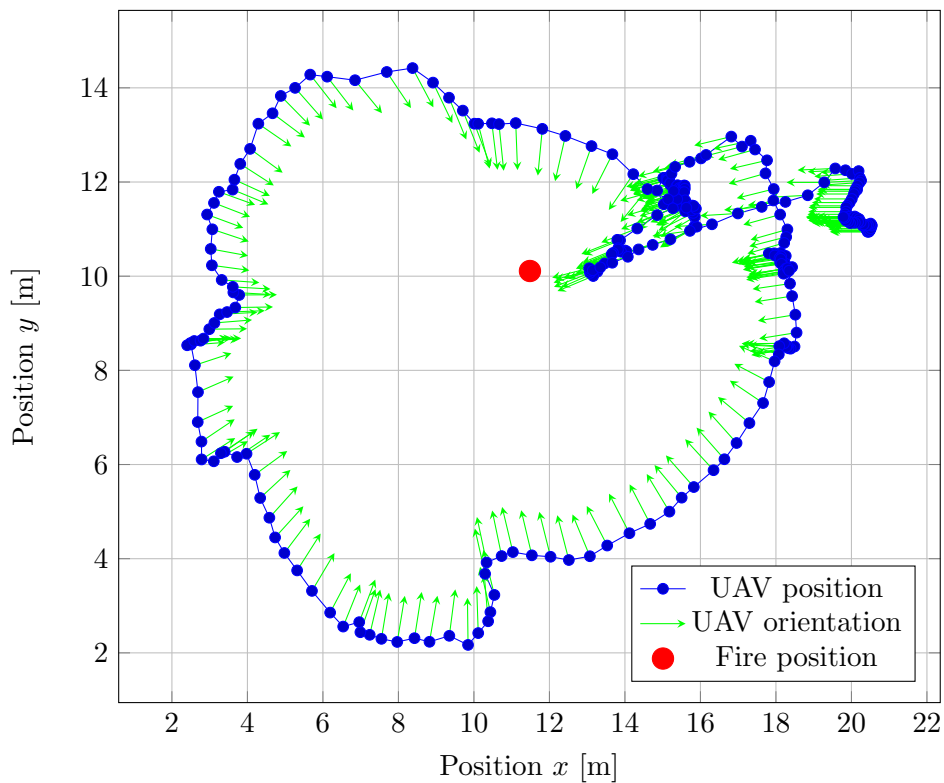

Figure 5.6: The followed trajectory of the UAV during the real-world experiment – circulation of the UAV around a static fire.

5.3.1   Fire classification

The quantitative evaluation of this experiment is summarized in the confusion matrix shown in Table 5.3. The results are compared to the ground truth data – manually labeled images. The data show the capabilities of the system to detect unknown fires from onboard

sensors with the detection accuracy of 0.939. Given the classification characteristics in Table 5.4, the performance of the system is robust to real-world inference and yields sufficient accuracy in non-simulated conditions.

	Hypothesis	
	positive	negative
Fire present	$TP = 2963$	$FN = 160$
Fire not present	$FP = 60$	$TN = 433$

Table 5.3: Confusion matrix as quantitative evaluation of the real-world experiment. Showing robust fire detector.

Characteristic	Description	Value
prediction accuracy	$ACC = \frac{TP+TN}{TP+TN+FP+FN}$	0.939
prediction error	$ERR = \frac{FP+FN}{TP+TN+FP+FN}$	0.061
false positive rate	$FPR = \frac{FP}{FP+TN}$	0.122
true positive rate = recall	$TPR = \frac{TP}{FN+TP}$	0.949
true negative rate	$TNR = \frac{TN}{FP+TN}$	0.878
precision	$PRE = \frac{TP}{TP+FP}$	0.980

Table 5.4: Qualitative characteristics of the detector measured during the real world experiment.

5.3.2 Fire localization

The fire localization accuracy is described by RMSE error and the absolute error histogram for position error of localized hypotheses. The histogram of absolute localization errors is given in Figure 5.7. The RMSE in the experiment (see Figure 5.6) is 2.39 m. In contrast to simulation experiments (see Section 5.2), the RMS error is significantly higher. There are several technical issues influencing this performance. These issues are a high time delay between the thermal and depth camera image streams. The thermal camera is asynchronously delayed by delay ranging from 1 s to 2 s. The time desynchronization with unknown image stream delay, together with the accuracy of the UAV pose estimation module, increase the localization error in real-world conditions. To improve the accuracy of the system, a low-latency thermal camera should be used onboard the UAV. This remains as part of a future work.
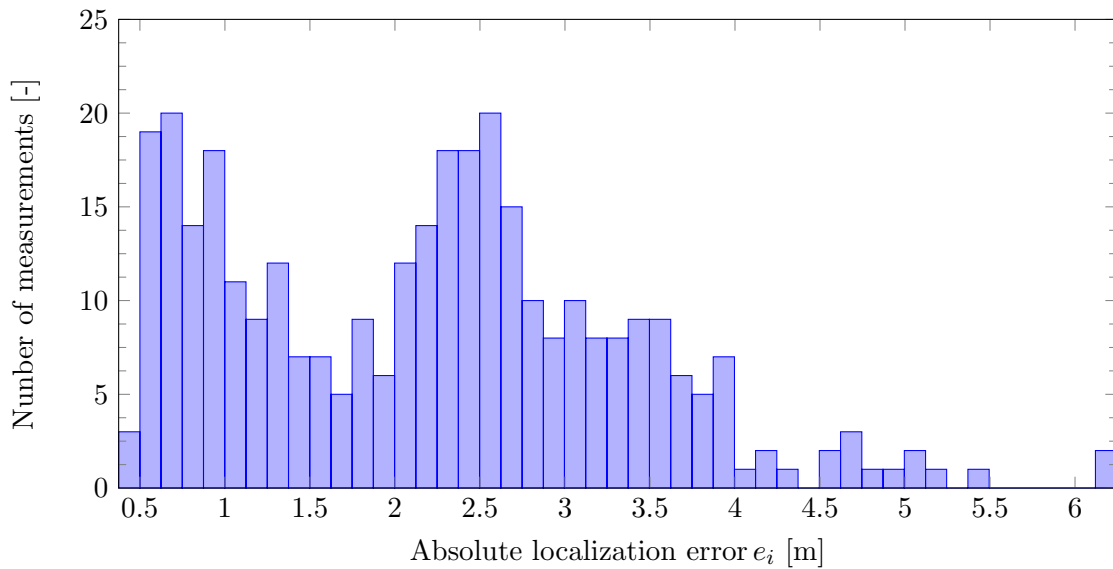

Figure 5.7: Histogram of the absolute error of the fire localization system. During a real-world flight, the system shows the ability to localize a fire in the world with RMSE 2.39 m.

5.3.3 Fire locking

The fire locking system estimates the optimal position with respect to a detected fire and the ballistic curve of the launched fire extinguishing charge. The proposed strategy (see Section 4.3) for UAV positioning uses the current lateral position and estimates only the heading and altitude of the UAV (and hence the launcher). Using a ballistic curve with parameters estimated later in Section 5.3.5, the performance of the system to estimate the optimal position is evaluated in this section. Figure 5.8 shows the desired (with respect to the current lateral position of the UAV) and the estimated altitude and heading. The data show low-error in the estimation of the optimal heading of the launcher. This is expected as the change in heading was slow during the experiment, hence reducing the influence of thermal camera delay on the estimation. On the other hand, the estimation of altitude is influenced by the projection of the image detections to 3D using depth camera data. The extremely noisy real-world depth data, together with thermal camera delay decrease the accuracy of the

localization and hence negatively influences the estimation of the optimal UAV position for launching. The data also show potential for filtration (such as average window, median filter, or Kalman filtering), which might increase the accuracy of the fire localization. This remains a part of future work.
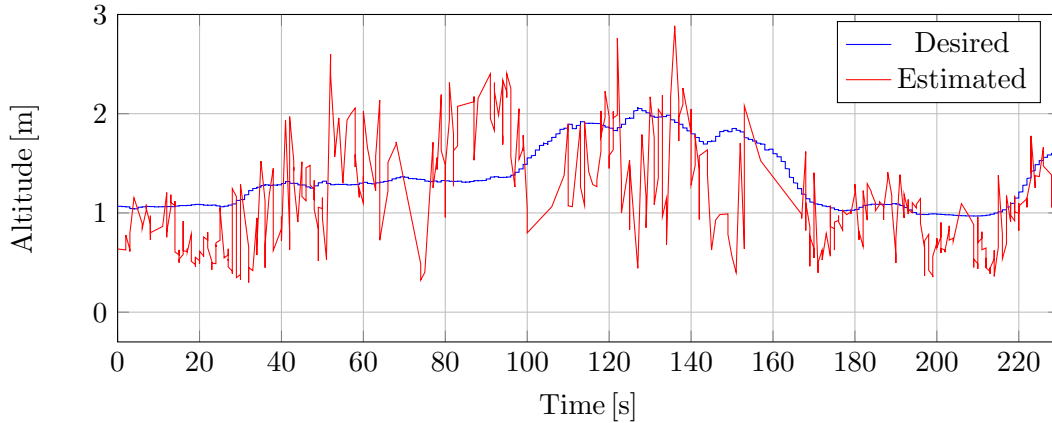
(a) Altitude estimation.
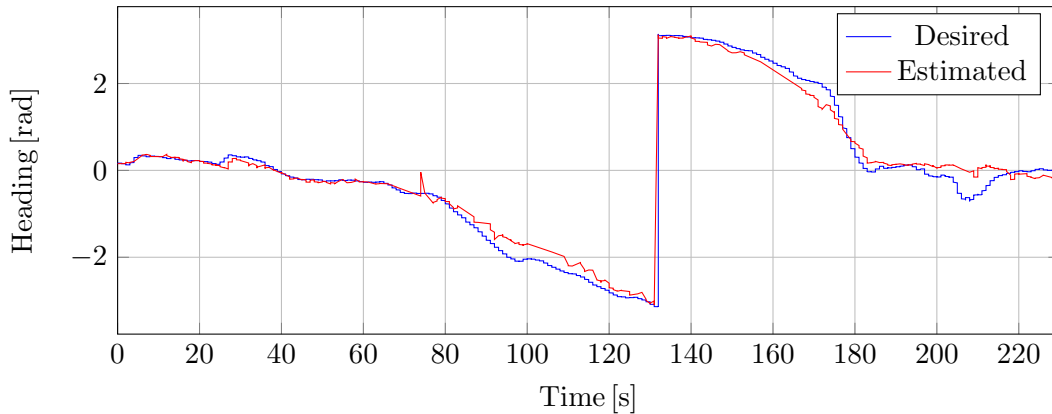
(b) Heading estimation.

Figure 5.8: Position estimation in the real experiment (see Figure 5.2). The UAV positioning system estimates the desired altitude and heading, while keeping the lateral position static.

5.3.4 Validation of the ampoule launcher

The launcher was manufactured and provided by an external provider. Initial ground tests have proved the capabilities of the launcher to discharge $0.5\,\mathrm{kg}$ charges to a distance of about $10\,\mathrm{m}$. The launcher was also tested onboard a flying UAV (see Figure 5.9). The results show the capabilities of the UAV to handle the dynamic recoil arising from the onboard discharging. The force produced by the ampoule discharge in the negative x-axis of the launcher is fastly suppressed by the motors capable of high-thrust production – the maximum position error reached $0.76\,\mathrm{m}$. During the experiment, the fire extinguishing ampoule was not available and hence was replaced by a $0.5\,\mathrm{l}$ water bottle (see Figure 5.9).

From an altitude of approximately 1.5 m, the discharged water bottle touched the ground after 14 m. The onboard discharge can be found within the multimedia materials available at `mrs.felk.cvut.cz/theses/nydrle2020`.

Figure 5.9: Fire extinguishing ampoule (replaced by water bottle in this experiment) discharged by the launcher.

5.3.5   Ballistic curve parameters estimation

As described in Section 4.3, the model of the ballistic curve requires two parameters to be estimated, namely v_0 (muzzle velocity) and h (coefficient of friction). This estimation is done from a sequence of photos of the discharge taken from a fixed point. The launcher coordination frame is projected to the fixed-camera frame and the coordinations $(l_{v,i}; l_{h,i})$ of the ampoule are estimated in different timestamps (see Figure 5.10). To estimate the ballistic curve parameters, the system of non-linear equations

$$l_{v,i} = \frac{gm}{v_0\,h} l_{h,i} + \frac{m^2 g}{h^2} \ln\left(1 - \frac{h l_{h,i}}{m\,v_0}\right), \forall i \in \{1, \cdots, N\}, \tag{5.3}$$

is solved, where N is the number of measured points. To find the solution of the above system of non-linear equations, the trust-region algorithm for solving nonlinear least-squares method [78] was used. Given the testing ampoule (a water bottle) with mass $m = 0.557\,\text{kg}$, the ballistic curve parameters $v_0 = 22.978\,\text{m}\,\text{s}^{-1}$ and $h = 0.129\,\text{kg}\,\text{s}^{-1}$ were estimated.
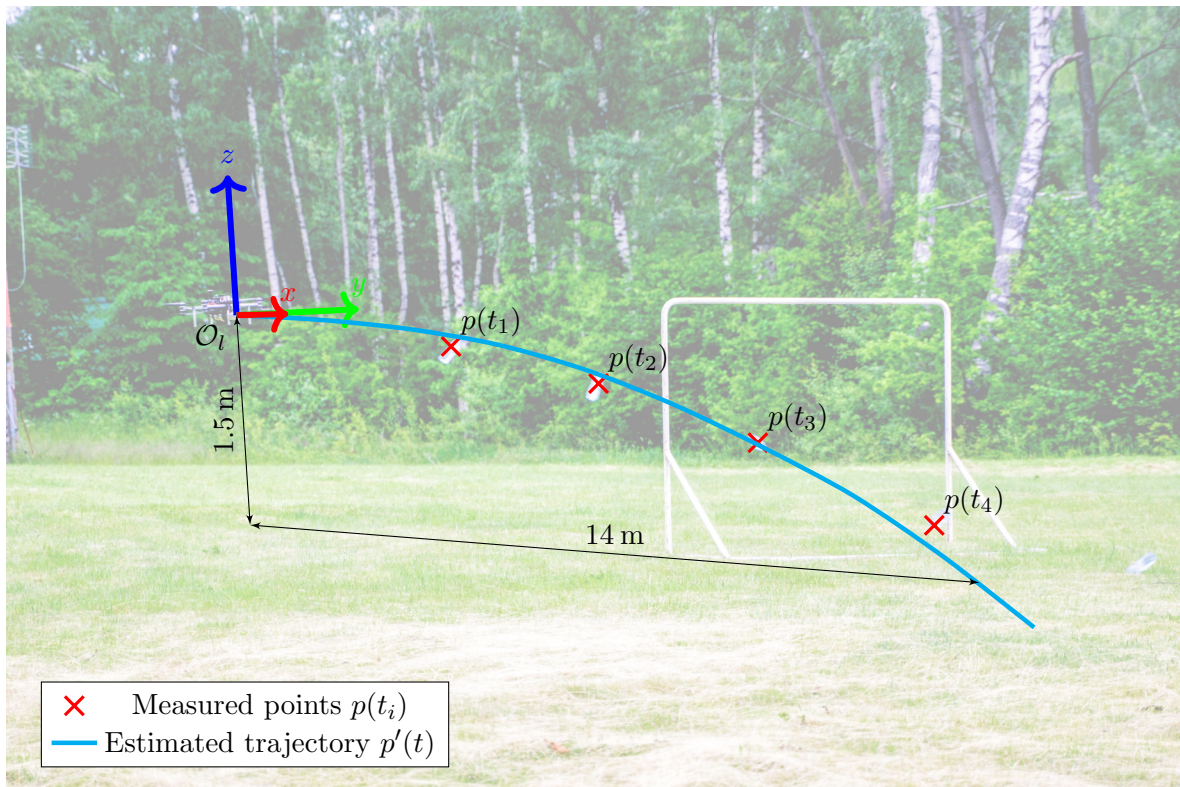
Figure 5.10: Estimated trajectory of the discharged ampoule from a set of measured ampoule positions using a static camera. $\mathcal{O}_l$ is the launcher coordination frame and $p(t)$ are the measured positions of the ampoule in time t.

Chapter 6: Conclusion

Contents

In this thesis, the design and construction of a specialized UAV adapted for aerial discharge of fire extinguishing ampoule is discussed. This thesis also designs, implements, and discusses the methods and algorithms for fire detection and localization. This was designed to help the human operator with finding fire sources as well as with the positioning of the UAV in order to launch the ampoule into a fire detected from onboard sensors and localized with respect to the UAV position.

In this thesis, the tasks given by the following list were successfully completed. The thesis is also supported by multimedia materials available at `mrs.felk.cvut.cz/theses/nydrle2020`.

- Chapter 3 describes the design and construction of the UAV platform that respects the requirements of the dynamic influence originating from horizontal discharging of an onboard payload.

- A launcher for discharging fire extinguishing capsules was integrated onto the designed aerial platform. The launcher was experimentally tested on-board the UAV.

- An algorithm detecting fires from an onboard thermal camera was designed in Section 4.1 and successfully tested in simulated and real-world conditions in Chapter 5.

- An algorithm autonomously positioning the UAV in order to launch the fire extinguishing capsules into a detected fire was designed in Section 4.3. The detected fire is localized using the algorithm developed in Section 4.2. The quality of these methods was tested in simulation and real-world conditions. The performance of the system is likewise discussed in Chapter 5.

- Both algorithms were implemented as ROS node interfacing with the system of Multi-Robot Systems group for stabilization and control of UAVs closely described in Section 2.4.

The fire localization subsystem has been tested in the Gazebo simulator where it demonstrated satisfactory results. However, these results were not repeated during the real-world experiment since the thermal camera used in this design produces thermal images with indispensable latency, causing desynchronization between thermal and depth image that leads to a large localization error while the UAV is moving.

6.1   Future work

Throughout the thesis, several drawbacks of the designed technical methodology were presented. Foremost, the time latency and time desynchronization of thermal and depth data reduced the accuracy of the fire localization system. This can be solved by employing a low-latency thermal camera.

The work can be further extended by the introduction of an easy-to-use user interface providing real-time reasoning over the on-board sensors' data. This may serve as an information stream for the human operator helping with assessing the situation.

Last but not least, the UAV positioning system should take into account the obstacles between the desired launching position and the heat source. A procedure detecting obstacles mid-way on the ballistic curve (such as window frames) should use this information to alter the 3D position of the UAV such that the fire extinguishant can be safely launched to the fire.

Bibliography

[1] A. D. Team. (2019) Octorotor X8 configuration. Accessed on March 21, 2019. [Online]. Available: http://ardupilot.org/copter/docs/connect-escs-and-motors.html# connect-escs-and-motors3

[2] S. for All Markus Mueller. (2019) eCalc online tool (free non-commercial license). Accessed on April 27, 2020. [Online]. Available: https://www.ecalc.ch/

[3] BONPET LIQUID | Bonpet systems. Accessed on April 12, 2020. [Online]. Available: https://www.bonpet.si/en_US/bonpet-tekocina

[4] (2015) Bonpet Grenade | Fire Defender. Accessed on April 12, 2020. [Online]. Available: http://www.fire-defender.com/en/bonpet-3/1465-2/

[5] B. Menkus, "A high rise building fire case study," *Computers & Security*, vol. 11, no. 1, pp. 19 – 23, 1992.

[6] A. Cowlard, W. Jahn, C. Abecassis-Empis, G. Rein, and J. L. Torero, "Sensor Assisted Fire Fighting," *Fire Technology*, vol. 46, no. 3, pp. 719–741, Jul 2010.

[7] M. G. Genovesi, D. P. Tashkin, S. Chopra, M. Morgan, and C. McElroy, "Transient hypoxemia in firemen following inhalation of smoke," *Chest*, vol. 71, no. 4, pp. 441 – 444, 1977.

[8] W. Xiang, W. Xinxin, Z. Jianhua, F. Jianchao, S. Xiu, and Z. Dejun, "Monitoring the thermal discharge of hongyanhe nuclear power plant with aerial remote sensing technology using a UAV platform," in *2017 IEEE International Geoscience and Remote Sensing Symposium (IGARSS)*, 2017, pp. 2958–2961.

[9] D. Kim, J. Youn, and C. Kim, "Automatic fault recognition of photovoltaic modules based on statistical analysis of UAV thermography," *The International Archives of Photogrammetry, Remote Sensing and Spatial Information Sciences*, vol. 42, p. 179, 2017.

[10] T. Giitsidis, E. G. Karakasis, A. Gasteratos, and G. C. Sirakoulis, "Human and Fire Detection from High Altitude UAV Images," in *2015 23rd Euromicro International Conference on Parallel, Distributed, and Network-Based Processing*, 2015, pp. 309–315.

[11] V. Sherstjuk, M. Zharikova, and I. Sokol, "Forest Fire-Fighting Monitoring System Based on UAV Team and Remote Sensing," in *2018 IEEE 38th International Conference on Electronics and Nanotechnology (ELNANO)*, 2018, pp. 663–668.

[12] D. W. Casbeer, R. W. Beard, T. W. McLain, Sai-Ming Li, and R. K. Mehra, "Forest fire monitoring with multiple small UAVs," in *Proceedings of the 2005, American Control Conference, 2005.*, 2005, pp. 3530–3535 vol. 5.

[13] L. Merino, F. Caballero, J. R. M. de Dios, I. Maza, and A. Ollero, "Automatic forest fire monitoring and measurement using unmanned aerial vehicles," in *Proceedings of the 6th International Congress on Forest Fire Research*, 2010.

[14] A. Koltunov and S. Ustin, "Early fire detection using non-linear multitemporal prediction of thermal imagery," *Remote Sensing of Environment*, vol. 110, no. 1, pp. 18 – 28, 2007.

[15] C. Kuenzer, C. Hecker, J. Zhang, S. Wessling, and W. Wagner, "The potential of multidiurnal modis thermal band data for coal fire detection," *International Journal of Remote Sensing*, vol. 29, no. 3, pp. 923–944, 2008.

[16] M. I. Chacon-Murguia and F. J. Perez-Vargas, "Thermal Video Analysis for Fire Detection Using Shape Regularity and Intensity Saturation Features," in *Pattern Recognition*, J. F. Martínez-Trinidad, J. A. Carrasco-Ochoa, C. Ben-Youssef Brants, and E. R. Hancock, Eds. Berlin, Heidelberg: Springer Berlin Heidelberg, 2011, pp. 118–126.

[17] D. Pozo, F. Olrno, and L. Alados-Arboledas, "Fire detection and growth monitoring using a multitemporal technique on avhrr mid-infrared and thermal channels," *Remote Sensing of Environment*, vol. 60, no. 2, pp. 111 – 120, 1997.

[18] C. Yuan, Z. Liu, and Y. Zhang, "Fire detection using infrared images for UAV-based forest fire surveillance," in *2017 International Conference on Unmanned Aircraft Systems (ICUAS)*, 2017, pp. 567–572.

[19] J.-H. Kim and B. Y. Lattimer, "Real-time probabilistic classification of fire and smoke using thermal imagery for intelligent firefighting robot," *Fire Safety Journal*, vol. 72, pp. 40 – 49, 2015.

[20] C. Yuan, Z. Liu, and Y. Zhang, "UAV-based forest fire detection and tracking using image processing techniques," in *2015 International Conference on Unmanned Aircraft Systems (ICUAS)*, 2015, pp. 639–643.

[21] N. Kalatzis, M. Avgeris, D. Dechouniotis, K. Papadakis-Vlachopapadopoulos, I. Roussaki, and S. Papavassiliou, "Edge Computing in IoT Ecosystems for UAV-Enabled Early Fire Detection," in *2018 IEEE International Conference on Smart Computing (SMARTCOMP)*, 2018, pp. 106–114.

[22] S. Sudhakar, V. Vijayakumar, C. Sathiya Kumar, V. Priya, L. Ravi, and V. Subramaniyaswamy, "Unmanned aerial vehicle (uav) based forest fire detection and monitoring for reducing false alarms in forest-fires," *Computer Communications*, vol. 149, pp. 1 – 16, 2020.

[23] Y. Zhao, J. Ma, X. Li, and J. Zhang, "Saliency Detection and Deep Learning-Based Wildfire Identification in UAV Imagery," *Sensors*, vol. 18, no. 3, p. 712, Feb 2018.

[24] C.-B. Liu and N. Ahuja, "Vision based fire detection," in *Proceedings of the 17th International Conference on Pattern Recognition, 2004. ICPR 2004.*, vol. 4. IEEE, 2004, pp. 134–137.

[25] S. Verstockt, A. Vanoosthuyse, S. Van Hoecke, P. Lambert, and R. Van de Walle, "Multi-sensor Fire Detection by Fusing Visual and Non-visual Flame Features," in *Image and Signal Processing*, A. Elmoataz, O. Lezoray, F. Nouboud, D. Mammass, and J. Meunier, Eds. Berlin, Heidelberg: Springer Berlin Heidelberg, 2010, pp. 333–341.

[26] H. Amano, K. Osuka, and T. . Tarn, "Development of vertically moving robot with gripping handrails for fire fighting," in *Proceedings 2001 IEEE/RSJ International Conference on Intelligent Robots and Systems. Expanding the Societal Role of Robotics in the the Next Millennium (Cat. No.01CH37180)*, vol. 2, 2001, pp. 661–667 vol.2.

[27] M. D. Montaigne and B. Lietaer, "High-rise fire fighting and rescue system," Sep. 12 1989, uS Patent 4,865,155.

[28] I.-C. Ho, "High rise building fire escape/fire fighting and building maintenance system," Dec. 19 1989, uS Patent 4,887,694.

[29] T. J. Bisson, "Ground and airborne fire fighting system and method of fighting high rise building fires," Aug. 4 1992, uS Patent 5,135,055.

[30] K. A. Ghamry, M. A. Kamel, and Y. Zhang, "Multiple UAVs in forest fire fighting mission using particle swarm optimization," in *2017 International Conference on Unmanned Aircraft Systems (ICUAS)*, 2017, pp. 1404–1409.

[31] K. Satish and N. Kishan, *Using UAV Technologies for Fire Fighting.* F9 Info. Technologies (P) Limited.

[32] J. Moore, "UAV Fire-fighting System," May 30 2013, uS Patent App. 13/306,419.

[33] B. Aydin, E. Selvi, J. Tao, and M. J. Starek, "Use of fire-extinguishing balls for a conceptual system of drone-assisted wildfire fighting," *Drones*, vol. 3, no. 1, p. 17, 2019.

[34] A. Imdoukh, A. Shaker, A. Al-Toukhy, D. Kablaoui, and M. El-Abd, "Semi-autonomous indoor firefighting UAV," in *2017 18th International Conference on Advanced Robotics (ICAR)*, 2017, pp. 310–315.

[35] A. I. N. Alshbatat, "Fire extinguishing system for high-rise buildings and rugged mountainous terrains utilizing quadrotor unmanned aerial vehicle," *International Journal of Image, Graphics and Signal Processing*, vol. 12, no. 1, p. 23, 2018.

[36] M. Vrba, D. Heřt, and M. Saska, "Onboard Marker-Less Detection and Localization of Non-Cooperating Drones for Their Safe Interception by an Autonomous Aerial System," *IEEE Robotics and Automation Letters*, vol. 4, no. 4, pp. 3402–3409, 2019.

[37] D. A. Saikin, T. Baca, M. Gurtner, and M. Saska, "Wildfire Fighting by Unmanned Aerial System Exploiting Its Time-Varying Mass," *IEEE Robotics and Automation Letters*, vol. 5, no. 2, pp. 2674–2681, 2020.

[38] D. Heřt, "Autonomous Predictive Interception of a Flying Target by an Unmanned Aerial Vehicle," Master's thesis, CZECH TECHNICAL UNIVERSITY IN PRAGUE, 2018.

[39] M. Vrba and M. Saska, "Marker-Less Micro Aerial Vehicle Detection and Localization Using Convolutional Neural Networks," *IEEE Robotics and Automation Letters*, vol. 5, no. 2, pp. 2459–2466, 2020.

[40] Z. Qin, J. Wang, and Y. Lu, "Triangulation Learning Network: From Monocular to Stereo 3D Object Detection," in *2019 IEEE/CVF Conference on Computer Vision and Pattern Recognition (CVPR)*, 2019, pp. 7607–7615.

[41] P. Li, X. Chen, and S. Shen, "Stereo r-cnn based 3d object detection for autonomous driving," in *Proceedings of the IEEE/CVF Conference on Computer Vision and Pattern Recognition (CVPR)*, June 2019.

[42] U.-P. Käppeler, M. Höferlin, and P. Levi, "3d object localization via stereo vision using an omnidirectional and a perspective camera," in *Proceedings of the 2nd Workshop on Omnidirectional Robot Vision, Anchorage, Alaska*. Citeseer, 2010.

[43] Pedram Azad, Tamim Asfour, and R. Dillmann, "Stereo-based 6D object localization for grasping with humanoid robot systems," in *2007 IEEE/RSJ International Conference on Intelligent Robots and Systems*, 2007, pp. 919–924.

[44] T. Baca, P. Stepan, and M. Saska, "Autonomous Landing On A Moving Car With Unmanned Aerial Vehicle," in *The European Conference on Mobile Robotics (ECMR)*, 2017.

[45] G. Loianno, V. Spurny, T. Baca, J. Thomas, D. Thakur, T. Krajnik, A. Zhou, A. Cho, M. Saska, and V. Kumar, "Localization, Grasping, and Transportation of Magnetic Objects by a team of MAVs in Challenging Desert like Environments," *IEEE Robotics and Automation Letters*, 2018.

[46] V. Spurny, T. Baca, M. Saska, R. Penicka, T. Krajnik, J. Thomas, D. Thakur, G. Loianno, and V. Kumar, "Cooperative Autonomous Search, Grasping and Delivering in a Treasure Hunt Scenario by a Team of UAVs," *Published in Journal of Field Robotics*, 2018.

[47] P. Petráček, V. Krátký, and M. Saska, "Dronument: System for reliable deployment of micro aerial vehicles in dark areas of large historical monuments," *IEEE Robotics and Automation Letters*, vol. 5, no. 2, pp. 2078–2085, April 2020.

[48] P. Petráček, "Design, Localization and Position Control of a Specialized UAV Platform for Documentation of Historical Monuments," Master's thesis, CZECH TECHNICAL UNIVERSITY IN PRAGUE, 2019.

[49] T. Baca, D. Hert, G. Loianno, M. Saska, and V. Kumar, "Model Predictive Trajectory Tracking and Collision Avoidance for Reliable Outdoor Deployment of Unmanned Aerial Vehicles," in *2018 IEEE/RSJ International Conference on Intelligent Robots and Systems (IROS)*. IEEE, 2018, pp. 1–8.

[50] B. M. Đ. and P. D. J., "A new curve for temperature-time relationship in compartment fire," *Thermal Science*, 2011.

[51] (2020) U1 || KV80. Accessed on April 27, 2020. [Online]. Available: http://store-en.tmotor.com/goods.php?id=731

[52] (2020) V505 KV260. Accessed on April 27, 2020. [Online]. Available: http://store-en.tmotor.com/goods.php?id=921

[53] L. Joseph and J. Cacace, *Mastering ROS for Robotics Programming: Design, build, and simulate complex robots using the Robot Operating System, 2nd Edition.* Packt Publishing, 2018.

[54] N. Koenig and A. Howard, "Design and use paradigms for Gazebo, an open-source multi-robot simulator," in *2004 IEEE/RSJ International Conference on Intelligent Robots and Systems (IROS) (IEEE Cat. No.04CH37566)*, vol. 3, 2004, pp. 2149–2154 vol.3.

[55] V. Pritzl, "UAV guidance for fire challenge of MBZIRC contest," Master's thesis, CZECH TECHNICAL UNIVERSITY IN PRAGUE, 2020.

[56] T. Baca, D. Hert, G. Loianno, M. Saska, and V. Kumar, "Model predictive trajectory tracking and collision avoidance for reliable outdoor deployment of unmanned aerial vehicles," in *2018 IEEE/RSJ International Conference on Intelligent Robots and Systems (IROS)*. IEEE, 2018, pp. 1–8.

[57] B. Theys, G. Dimitriadis, P. Hendrick, and J. De Schutter, "Influence of propeller configuration on propulsion system efficiency of multi-rotor Unmanned Aerial Vehicles," in *2016 International Conference on Unmanned Aircraft Systems (ICUAS)*, June 2016, pp. 195–201.

[58] A. Yudhanto, N. Watanabe, Y. Iwahori, and H. Hoshi, "Effect of stitch density on tensile properties and damage mechanisms of stitched carbon/epoxy composites," *Composites Part B: Engineering*, vol. 46, pp. 151 – 165, 2013.

[59] D. L. Gabriel, J. Meyer, and F. du Plessis, "Brushless DC motor characterisation and selection for a fixed wing UAV," in *IEEE Africon '11*, 2011, pp. 1–6.

[60] (2012) KDE4215XF-465. Accessed on April 16, 2020. [Online]. Available: https://www.kdedirect.com/collections/uas-multi-rotor-brushless-motors/products/kde4215xf-465

[61] (2020) P15x5 Prop-2PCS/PAIR. Accessed on April 16, 2020. [Online]. Available: http://store-en.tmotor.com/goods.php?id=381

[62] (2020) Pixhawk 4. Accessed on April 14, 2020. [Online]. Available: https://docs.px4.io/v1.9.0/en/flight_controller/pixhawk4.html

[63] (2019) WIRIS® Pro. Accessed on April 30, 2020. [Online]. Available: https://www.drone-thermal-camera.com/products/workswell-wiris-pro-uav-thermal-imaging-camera-for-industry/

[64] (2018) video_stream_opencv. ROS. Accessed on April 28, 2020. [Online]. Available: http://wiki.ros.org/video_stream_opencv

[65] Intel® RealSense™ Depth Camera D435i. Accessed on April 1, 2020. [Online]. Available: https://www.intelrealsense.com/depth-camera-d435i/

[66] Neo-M8 u-blox M8 concurrent GNSS modules data sheet. Accessed on April 27, 2020. [Online]. Available: https://www.u-blox.com/sites/default/files/NEO-M8-FW3_DataSheet_%28UBX-15031086%29.pdf

[67] J. Lloyd, *Thermal Imaging Systems*, ser. Optical Physics and Engineering.   Springer US, 2013.

[68] N. I. Furashov, V. Y. Katkov, and B. A. Sverdlov, "Submillimetre spectrum of the atmospheric water vapour absorption-some experimental results," in *1989 Sixth International Conference on Antennas and Propagation, ICAP 89 (Conf. Publ. No.301)*, 1989, pp. 310–312 vol.2.

[69] A. Gardecka, "Synthesis and characterisation of niobium doped tio2 semiconducting materials," 11 2016.

[70] J. Silvela and J. Portillo, "Breadth-first search and its application to image processing problems," *IEEE Transactions on Image Processing*, vol. 10, no. 8, pp. 1194–1199, 2001.

[71] S. H. Lee and S. Sharma, "Real-time disparity estimation algorithm for stereo camera systems," *IEEE Transactions on Consumer Electronics*, vol. 57, no. 3, pp. 1018–1026, 2011.

[72] H. Richard, *Multiple view geometry in computer vision / Richard Hartley, Andrew Zisserman*, second edition ed.   Cambridge: Cambridge University Press, 2003.

[73] P. F. Sturm and S. J. Maybank, "On plane-based camera calibration: A general algorithm, singularities, applications," in *Proceedings. 1999 IEEE Computer Society Conference on Computer Vision and Pattern Recognition (Cat. No PR00149)*, vol. 1, 1999, pp. 432–437 Vol. 1.

[74] W. Hackborn, "Projectile motion: Resistance is fertile," *American Mathematical Monthly*, vol. 115, pp. 813–819, 11 2008.

[75] Q. Jia, X. Li, J. Song, X. Gao, G. Chen, and H. Zhang, "Projectile motion aerodynamic parameter identification and simulation," in *2014 9th IEEE Conference on Industrial Electronics and Applications*, 2014, pp. 1872–1876.

[76] V. V. Chistyakov and K. S. Malykh, "A precise parametric equation for the trajectory of a point projectile in the air with quadratic drag and longitudinal or side wind," in *2015 International Conference on Mechanics - Seventh Polyakhov's Reading*, 2015, pp. 1–5.

[77] S. Raschka, "An Overview of General Performance Metrics of Binary Classifier Systems," 2014.

[78] N. I. M. Gould and P. L. Toint, "Filtrane, a fortran 95 filter-trust-region package for solving nonlinear least-squares and nonlinear feasibility problems," *ACM Trans. Math. Softw.*, vol. 33, no. 1, p. 3–es, Mar. 2007.

Appendices

CD Content

Table 1 lists arrangement of directories on the attached CD.

Directory name	Description
thesis.pdf	the thesis in pdf format
sources/thesis	latex source codes
sources/fire_localization	software source codes
CAD_model.zip	model of the designed UAV
media	multimedia materials

Table 1: CD Content.

List of abbreviations

Table 2 lists abbreviations used in this thesis.

Abbreviation	Meaning
UAV	Unmanned Aerial Vehicle
FEE CTU	Faculty of Electrical Engineering, Czech Technical University in Prague
MRS	Multi-Robot Systems group at FEE CTU
FPV	First Person View
ROS	Robot Operating System
TCP	Transmission Control Protocol
MBZIRC	Mohamed Bin Zayed International Robotics Challenge
GPS	Global Positioning System
GNSS	Global Navigation Satellite System
ESC	Electronic Speed Controller
LiPo	Lithium-Polymer accumulator
PCB	Printed Circuit Board
LiDAR	Light Detection and Ranging
PWM	Pulse Width Modulation
IMU	Inertial Measurement Unit
USB	Universal Serial Bus
EM	Electromagnetic
IR	Infra-red
FoV	Field of View
RMSE	Root Mean Squared Error

Table 2: Lists of abbreviations.